Crystal Chemistry of Thallium in Marine Ferromanganese Deposits

Alain Manceau, Alexandre Simionovici, Nathaniel Findling, Pieter Glatzel, Blanka Detlefs, Anna Wegorzewski, Kira Mizell, James Hein, Andrea Koschinsky

Crystal Chemistry of Thallium in Marine Ferromanganese Deposits

Alain Manceau*[1], Alexandre Simionovici[1], Nathaniel Findling[1], Pieter Glatzel[2], Blanka Detlefs[2], Anna V. Wegorzewski[3], Kira Mizell[4], James R. Hein[4], and Andrea Koschinsky*[5]

[1]Université Grenoble Alpes, ISTerre, CNRS, CS40700, F-38058 Grenoble, France

[2]European Synchrotron Radiation Facility (ESRF), F-38000 Grenoble, France

[3]Federal Institute for Geoscience and Natural Resources (BGR), Stilleweg 2, D-30655 Hannover, Germany

[4]U.S. Geological Survey, Pacific Coastal and Marine Science Center, Santa Cruz, California 95060, United States

[5]Department of Physics and Earth Sciences, Jacobs University Bremen, Bremen 28759, Germany

*Corresponding Authors : alain.manceau@univ-grenoble-alpes.fr; a.koschinsky@jacobs-university.de

ABSTRACT

Our understanding of the up to seven orders of magnitude partitioning of thallium (Tl) between seawater and ferromanganese (FeMn) deposits rests upon two foundations: (1) being able to quantify the Tl(I)/Tl(III) ratio that reflects the extent of the oxidative scavenging of Tl by vernadite (δ-MnO_2), the principle manganate mineral in oxic and suboxic environments, and (2) being able to determine the sorption sites and bonding environments of the Tl(I) and Tl(III) complexes on vernadite. We investigated these foundations by determining the oxidation state and chemical form of Tl in FeMn crusts and nodules from the global oceans at a Tl concentration ranging from several hundreds ppm (mg/kg) down to the low ppm level. Seventeen hydrogenetic crusts and eleven nodules from the Pacific, Atlantic, and Indian oceans and Baltic Sea were characterized by chemical analysis, X-ray diffraction, Raman spectroscopy, Mn K-edge X-ray absorption near-edge structure (XANES) spectroscopy, and Tl L_3-edge high energy-resolution XANES (HR-XANES) and extended X-ray absorption fine structure (EXAFS) spectroscopy. The Tl concentration increases linearly from 1.5 to 319 ppm with the Mn/Fe ratio in Fe-vernadite from hydrogenetic crusts, whereas the percentage of Tl(III) to total Tl varies between 62% and 100% independent of both the Mn/Fe and Mn(III)/Mn(IV)

ratios. The data, complemented by molecular modeling of the Tl(III) coordination and by XANES calculations, suggest that the enrichment of Tl in Fe-vernadite is driven by (1) the oxidative uptake of octahedrally coordinated Tl(III) above the vacant Mn(IV) sites and on the layer edges of the vernadite layers, and (2) the sorption of Tl(I) on the crystallographic site of Ba at the surface of the vernadite layers, which is analog to the surface site of K. Thus, Tl has a high affinity for vernadite regardless of its oxidation state, and the lack of correlation between Tl(III) and the Mn/Fe ratio in FeMn crusts is explained by the affinity of Tl(I) for the Ba site. The Tl concentration varies between 2 and 112 ppm in surface and buried nodules independent of the Mn/Fe ratio, and the percentage of Tl(III) varies between 0% and 100%. Nodules subjected to sediment diagenesis with replacement of layered vernadite by tunneled todorokite are depleted in Tl and have more reduced thallium. Knowledge of the complex interplay of mineralogy, surface chemical processes, and crystallographic siting are required to understand the variability of Tl concentrations, redox state, and acquisition processes by marine FeMn deposits.

KEYWORDS: EXAFS, XANES, X-ray diffraction, Raman spectroscopy, birnessite, vernadite, todorokite

INTRODUCTION

Thallium (Tl) is enriched in ferromanganese (FeMn) crusts and nodules that cover the surface of seamounts and seafloors throughout the oceans.[1–4] The average Tl contents of nine major regions of the Pacific, Atlantic, and Indian oceans range from 129 to 347 ppm (mg/kg) in nodules and from 41 to 160 ppm in crusts.[5] Taking a mean dissolved Tl concentration of 65 pmol/kg in the global oceans,[3] the partitioning of Tl between seawater and FeMn crusts and nodules is as high as 10^7. The enrichment of Tl in marine FeMn deposits makes them a useful archive of Tl fluxes over the Cenozoic for which Tl isotopes have been interpreted as a proxy for organic carbon burial in the oceans.[6] In addition, FeMn minerals may be considered economically interesting as a resource for Tl. Thallium is classified as a strategic element because of its low natural abundance and use in advanced technologies, including electronics, optics, and HT-superconductors. Currently, the main source of mineable Tl is the trace amounts occurring in Cu (chalcopyrite), Pb (galena), Zn (sphalerite), and other sulfide ores. The concentration of Tl in commonly exploited sulfide ores is about 100 ppm (mg/kg),[7] which is met or surpassed by the mean concentrations in marine FeMn minerals. Determining the enrichment

mechanisms, phase associations, and coordination chemistry of Tl in FeMn crusts and nodules has implications for both paleoceanographic and resource evaluations.

State of knowledge for thallium enrichment in manganese oxides. It is considered that Mn-associated Tl enrichment in marine deposits and soils results from the oxidative scavenging of Tl(I) to Tl(III) in contact with phyllomanganates of the birnessite group (MnO_{2-x}).[8–14] A single micro-XANES study of a hydrogenetic crust from the Pacific Ocean performed in 2012 by Peacock and Moon[9] showed that Tl, associated spatially with turbostratic (i.e., *c*-disordered[15]) birnessite (δ-MnO_2, named vernadite[16–20]) and with todorokite,[21] occurred in both 1+ and 3+ oxidation states. As much as 58 ± 3% of Tl was 1+ despite the oxic formation environment of FeMn crusts. This conundrum is informed by laboratory experiment, which shows that the $Tl(I)_{(aq)} \rightarrow Tl(III)_{(s)}$ oxidation occurs only when birnessite is depleted in Mn^{3+}, and does not occur at all on todorokite,[9,11] because this tectomanganate is naturally rich in Mn^{3+}.[22,23] These findings suggest that the Tl(III)/Tl(I) ratio could be a powerful tracer of the Mn(IV)/Mn(III) ratio and vice versa, the manganate mineralogy, and the redox conditions of the geochemical setting. Thus, precise knowledge of the oxidation states of Mn and Tl and identity of the Tl-carrying phases is essential to advance research on geochemical processes responsible for the enrichment of Tl in marine deposits.

Understanding the structure of the Tl(III) surface complex on vernadite is also a necessary prerequisite to model the $Tl(I)_{(aq)} \rightarrow Tl(III)_{(s)}$ redox reaction and to understand the key role of Mn^{3+} in this reaction. Extended X-ray absorption fine structure (EXAFS) studies of Tl sorption on δ-MnO_2 showed that Tl(I) is oxidized to Tl(III) primarily on vacancy sites of the MnO_2 layer as a tridentate corner-sharing (TCS) complex with a Tl-Mn distance of 3.60-3.63 Å and secondarily on the edges of the layer as a double edge-sharing (DES) complex with a Tl-Mn distance of 3.27-3.28 Å (Figure 1).[9,11,12] The coordination of the Tl(III)-TCS complex derived from EXAFS has not been fully resolved. Two studies reported a split O coordination shell with *d*(Tl-O) = 2.15-2.18 Å and 2.23-2.26 Å interpreted as an elongated tetrahedral coordination over the Mn vacancies,[9,12] and one study reported a single bond distance of 2.20 Å interpreted as an octahedral coordination on both the vacancy and edge sites.[11]

Considerations for thallium X-ray absorption spectroscopy in marine ferromanganese minerals. The Tl concentration in the Peacock and Moon[9] study was as high as 2000 ppm, and even higher at the points of interest ($n = 4$) measured by micro-XANES spectroscopy. There is a clear need to extend this pioneering research in the range of a few hundred ppm down to several ppm that represent the typical concentrations of Tl in FeMn deposits from the global ocean. It is also desirable

to obtain the oxidation state of Tl in whole samples to ensure that observations made at the micrometer scale with point analyses are representative of the bulk. EXAFS data on marine vernadite is lacking, therefore there is no evidence that Tl-sorbed δ-MnO_2 surrogates represent how Tl(III) is taken up in FeMn marine deposits. We show below that information on the oxidation state and bonding environment of Tl is difficult to obtain on natural materials with standard XANES and EXAFS spectroscopy because of analytical challenges posed by the multi-elemental composition of Earth materials.

X-ray absorption spectra of elements in low concentrations are measured usually in fluorescence-yield detection mode using an energy-dispersive detector (EDS). An EDS has an energy bandwidth of about 150-200 eV at 10,000 eV, not high enough to separate the X-ray fluorescence lines for two or more elements in multi-element samples. This is particularly striking for Tl because of the proximity of the Tl L_3 (12,658 eV) and the As K (11,867 eV) *absorption edges*, and the resulting overlap of the Tl $L_{\alpha 1}$ (10,269 eV) and As $K_{\alpha 1,2}$ (10,508 – 10,543 eV) *fluorescence lines*. The Tl/As atomic ratio of the nine main FeMn deposits ranges between 1.09 and 0.06 (mean = 0.39 ± 0.38).[4] At [Tl] = 283 ppm and [As] = 151 ppm ($(Tl/As)_{at}$ = 0.69, sample MP23-2, Table 1), the Tl $L_{\alpha 1}$ line is half as intense as the $K_{\alpha 1,2}$ line (Figure 2a). Thus, the measurement is feasible with an EDS albeit with a degraded signal-to-noise ratio due to the high background signal from the parasitic As $K_{\alpha 1,2}$ fluorescence. In contrast, at [Tl] = 2 ppm and [As] = 302 ppm ($(Tl/As)_{at}$ = 0.002, sample BS-surface, Table 1), the Tl $L_{\alpha 1}$ line is totally shadowed by the intense As $K_{\alpha 1,2}$ line (Figure 2b), hampering the measurement of X-ray absorption spectra at low Tl concentration in natural FeMn oxides. Still, when measurement is feasible the EXAFS spectrum is limited to k_{max} = 9.9 $Å^{-1}$ by the Pb L_3-edge situated 377 eV above the absorption edge of Tl (Figure S1). The resolution in distance is $\Delta R = \pi/2k_{max}$ = 0.16 Å,[24] clearly not enough to detect a possible split of the oxygen shell.

Here, this analytical challenge was tackled by selecting the Tl $L_{\alpha 1}$ line using a wavelength dispersive spectrometer (WDS) consisting of five high-luminosity analyzer crystals.[25] A crystal analyzer acts both as a low-pass and high-pass filter, eliminating the undesired fluorescence lines at lower and higher energies (e.g., the As $K_{\alpha 1,2}$ and Pb L_α lines), and also the elastic and inelastic rays at higher energy. Notably, it filters the intense Fe and Mn $K_{\alpha 1,2}$ lines from the matrix (5900 and 6400 eV), which otherwise would saturate the detector. This is shown in Figure S2 with the BS-surface nodule which has 15.6 wt % Mn and 14.7 wt % Fe, and the MP23-2 crust which has 28.9 wt % Mn and 7.3 wt % Fe. The Mn and Fe $K_{\alpha 1,2}$ fluorescence lines are between two and three orders of magnitude more intense than the Tl $L_{\alpha 1}$ line. Filtering the Pb L_α line allows extending the *k*-range of EXAFS beyond the Pb L_3-

edge (Figure 2c and S1).[26] Another benefit of a spectrometer to study Tl is that the width of the diffracted $L_{\alpha 1}$ line is about four times lower than the core hole lifetime of the photoelectric X-ray absorption event (~1.5 eV vs ~6.0 eV).[27] As a consequence, the XANES structures are finely resolved when measured at high energy-resolution (HR-XANES) with a WDS,[28,29] whereas they are featureless when measured with an EDS.[9,30] Thus, HR-XANES provides better precision on the Tl(III)/Tl(I) ratio. In the field of mineralogy, HR-XANES (also designated HERFD-XANES[31]) has been applied previously to study the crystal chemistry of gold, arsenic, and selenium in pyrite and arsenopyrite,[32–35] uranium in phosphates,[36] and cobalt in Mn and Fe (oxyhydr)oxides and olivine.[37]

Organization of the paper. First, we present the composition, mineralogy and average Mn valence of 17 crusts and 11 nodules from the global ocean obtained by chemical analysis, X-ray diffraction (XRD), Raman spectroscopy, and Mn K-edge XANES spectroscopy. Then, we compare the XANES and HR-XANES spectra of a Tl(I) ($TlNO_3$) and a Tl(III) (Tl_2O_3) reference, and we assign the Tl_2O_3 spectral features with *ab initio* FEFF9.6[38] calculations. Next, the HR-XANES spectra of the 28 crusts and nodules are presented, analyzed by principal component analysis (PCA) and iterative target factor analysis (ITFA),[39–42] and the Tl(III)/Tl(I) ratios calculated using least-squares fitting (LSF) of the experimental HR-XANES spectra with linear combinations of the Tl(III) and Tl(I) endmember spectra obtained by ITFA. Finally, we describe and fit the EXAFS data of one crust to confirm the coordination environment of thallium in marine FeMn oxides. These data provide novel insights regarding (1) the coordination chemistry of Tl(III) on vernadite and the molecular model of the surface complexes, (2) the relationship between the oxidation states of Mn and Tl, (3) the identity of the Tl(I) carrier phase, and (4) the geochemical significance of the spectroscopic results with regard to sequestration of Tl in ferromanganese oxides over their million-year growth history and implications for the deposit model.

MATERIALS AND METHOD

FeMn oxide samples. Samples were recovered from a wide range of depositional settings from the Pacific, Atlantic, Indian, and Arctic oceans and the Baltic Sea to determine if Tl geochemistry and crystal chemistry vary regionally due to different geographic or oceanographic parameters (Tables 1 and S1). They include hydrogenetic FeMn crusts (i.e. precipitated from the water column) and diagenetic FeMn nodules (i.e. formed from biogeochemical processes in surface and buried sediments), as well as mixed hydrogenetic-diagenetic nodules from the Clarion Clipperton Zone (CCZ) in the northeast Pacific. The hydrogenetic crusts formed at extremely slow growth rates of only a few mm/Ma (million years) over periods of up to 70 Ma[5] while the fast growing shallow-water nodule from

the Baltic Sea formed at a rate of 0.2 mm/y and is only a few thousand years old.[43] The deepest crust and nodule samples were retrieved from >4000 m and the shallowest was collected from 20 m depth in the Baltic Sea. Most samples used here have already been investigated in previous studies and are hence rather well characterized with respect to formation and chemical and mineralogical compositions,[44–51] although Tl concentrations were not reported for all samples.

Hydrogenetic crusts from the Pacific were collected from water depths between about 1100 and 3049 m from various seamounts mostly in the central North and South Pacific Ocean.[52] While most hydrogenetic crusts were not affected by diagenetic phosphatization, three crust samples are included in which the older crust generation was phosphatized via impregnation and partial replacement by carbonate fluorapatite (CFA) under suboxic conditions.[53] The two crusts from the NE Atlantic are from different seamounts, the well-characterized Tropic Seamount, located approximately 470 km off Cape Blanc, West Africa, where thick crusts were influenced by terrigenous input[54–56] with ages up to 75 Ma,[57] and an unnamed seamount south of Tropic Seamount for which recovered crusts had not yet been described. The Arctic Ocean crusts show atypically high aluminosilicate detritus, Fe/Mn ratios, and growth rates compared to crusts formed elsewhere.[58]

The Indian Ocean crusts have growth rates comparable to Atlantic and Pacific ocean crust growth rates, but maximum crust ages are generally less than for thick Pacific and Atlantic crusts. One FeMn crust (SO92-74GTV) was collected at the Green Rock Hill in 2808 m water depth close to the Rodriguez Triple Junction in the central Indian Ocean. This crust sample formed on serpentinized ultramafic substrate as fallout from hydrothermal plumes at a high growth rate of about 20 mm/Ma and reduced contents of elements which are typically enriched in hydrogenetic crusts by oxidative scavenging such as Co and Ce.[46] The hydrothermal plume probably derived from the recently detected Kaimana vent field located about 17 km distance from the sample site (Schwarz-Schampera & Gibson, in prep).

The fast-growing shallow Baltic Sea nodule was collected from the southwestern part of the Baltic Sea, where nodules occur in about 20 m water depth as coatings up to several cm thick on pebbles.[43,59] A part of the selected sample was crushed as a bulk sample and another part only the upper mm of the surface was scraped off. The nodule SO79 KG1313 was recovered from an extended nodule field in the Peru Basin[60] at the southern rim of the equatorial high-productivity zone in the eastern Pacific, which explains the high growth rates of up to 250 mm/Ma and the strong diagenetic component compared to the nodules from the central Pacific Ocean within the CCZ which are mostly of mixed hydrogenetic-diagenetic origin. The CCZ nodules are growing on the sediment surface, the surface of

nodules is in contact with the near bottom sea water and the bottom side is buried within the upper few cm of the sediment. Those nodules are mainly mixed type nodules consisting of hydrogenetic as well as diagenetic origin.[48,61] The hydrogenetic growth structures form due to metal precipitation from the oxic near-bottom sea water as well as pore water and diagentic growth structures form due to metal precipitation from pore water under suboxic conditions. Furthermore, nodules buried within the sediment column down to even 10 m were found and included into this study (Table 1). Those nodules are diagenetically overprinted and differ in chemistry as well as mineralogy from those forming on the sediment surface.[51]

Chemical analysis. Crusts samples DODO 232D, RRKNOX06 D20-1A and D20-1B, HLY0905 DS4-003A, and AVON02 11-A were analyzed by SGS, Canada laboratory using XRF borate-fused disks for major elements; inductively coupled plasma mass spectrometry (ICP-MS) using lithium-metaborate fused disks for Cu, Mo, Ni, V, Zr, and Rare Earth elements plus Y (REY); ICP-MS following four-acid digest for all other trace elements. Further information regarding chemical analyses for the RRKNOX06 samples can be found in Hein et al.,[62] and for the HLY0905 sample in Hein et al.[58] All other samples were analysed in the geochemistry laboratory at Jacobs Univeristy Bremen using acid-pressure digestion and ICP analysis. Ground samples of FeMn crusts were dried at 105 °C for 24 h and then 0.05 g of sample powder was weighed into Teflon digestion vessels. The acid pressure digestion in a PicoTrace system was done using 3 mL HCl, 1 mL HNO_3 and 1 mL HF (all Merck suprapure quality). After evaporation of the liquid and twofold evaporation of 5 mL HCl, the residue was taken up in 50 mL of 0.5 M HNO_3/0.5% HCl. Major and minor elements in the FeMn nodules and crusts were measured using a Spectro Ciros Vision SOP ICP-OES, whereas trace elements including Tl were measured with a Perkin-Elmer Elan drc-e quadrupole ICP-MS. Arsenic and V were measured in a reaction cell in collision cell mode (KED mode) with helium gas, to eliminate interferences. Details of the digestion method, the analytical procedure and analytical uncertainties with common certified reference materials (CRM) are outlined by Dulski (2001)[63] and Alexander (2008).[64] Method reliability was verified by analysis of the CRM FeMn-1, JMn-1, and NODP1, which were digested and analyzed along with the FeMn crust and nodule samples. The analytical precision is better than ±5% of published reference values, except Al, Ba, V, some REY, Zr and W with an analytical precision of up to ±10%. Elemental compositions are reported in Table S2.

X-ray diffraction. 23 samples were characterized by XRD in this study and 5 were characterized previously (Table 1).[51] The new XRD patterns were recorded using a Bruker D8 Discover diffractometer with Cu Kα radiation (wavelength = 1.54 Å) from 5 to 71° 2θ, 0.06° step size, and 16 s

counting time. The samples with a basal reflection near 10 Å at ambient condition were dehydrated at 120 °C in vacuum during ~12 hours, then a new diffractogram was measured at ambient condition from 7 to 27° 2θ. This treatment allows differentiating 10 Å vernadite from todorokite.[23,51,65,66]

Raman spectroscopy. The black (i.e., manganese-rich) particles of hydrogenetic Fe-vernadite were subjected to Raman analysis to identify the mineralogical nature of the Fe-component. The analyses were performed using a Horiba XploRA plus (Jobin Yvon) confocal microscope equipped with a 532 nm laser. The spectra were acquired with 10x magnification objective lens at 1 mW laser power, using a 600 lines/mm grating and 30 s integration time. 10 spots were measured per sample to verify the repeatability of the data and were summed to enhance the signal to noise ratio. The background fluorescence was subtracted by linear interpolation of the intensity at 100 cm^{-1} and 1200 cm^{-1}.

Mn-XANES. The Mn K-edge XANES spectra were measured at room temperature in transmission mode on pressed pellets at the Swiss Norwegian BM31 beamlines[67] at the European Synchrotron Radiation Facility (ESRF) using the new extremely brilliant X-ray source (EBS). The flux on the sample was approximately 8×10^9 photon/s in a beam footprint of ~0.6 (V) x 5 (H) mm^2 FWHM. The photon energy was calibrated by assigning the maximum of the derivative of the Mn foil to be 6537.7 eV.[68] The stability in energy was monitored by measuring simultaneously to the samples the absorption signal of a Mn foil with an additional ion chamber on the downside of the experiment. The incident energy of the XANES spectra was scanned continuously from 6450 eV to 7000 eV in 0.2 eV steps and the spectra were normalized with Athena.[69]

The average oxidation state (AOS) of Mn was determined by LSF to an extended database of reference spectra under the constraint of non-negativity in the loadings (Combo fit[70]). The reference spectra were measured in transmission mode on diluted pellets during the same experimental session as the FeMn samples. The database is a transmission version of the one measured previously in total electron yield (TEY) mode.[70] It includes four Mn(IV) standards, five Mn(III) standards, and six Mn(II) standards (Table S3). The consistency between the transmission and TEY measurements was checked by remeasuring three mixed-valent tectomanganates, hollandite, psilomelane, and todorokite. The new AOS are systematically higher than the older ones by 0.04 valence unit (v.u.) for hollandite, 0.05 v.u. for psilomelane, and 0.06 v.u. for todorokite (Table 2). The accuracy of the Mn AOS was estimated to be equal to the variation of their best-fit values when the fit residual (*NSS*) was increased by 20%. *NSS* is the normalized sum-squared difference between the data and fit expressed as $\Sigma[(y_{data}-y_{fit})^2]/\Sigma(y_{data}^2)$. The precision on the variation of the Mn AOS between two samples is about one half as good as the accuracy of estimation (Figure S3).

Tl-XANES and EXAFS. The Tl L_3-edge HR-XANES and EXAFS spectra were measured on pressed pellets at the ID26 beamline of the ESRF using the EBS. The flux on the sample was over 10^{13} photon/s in a beam footprint of ~80 (V) x 80 (H) µm² FWHM. The Tl $L_{\alpha 1}$ ($3d_{5/2} \rightarrow 2p_{3/2}$) fluorescence line was selected using the 555 reflection of five Si crystals of 100 mm diameter and spherically bent to a radius of 0.5 m.[25] The Bragg angle was 74.3° in a vertical Rowland geometry. The diffracted intensity was measured with a Si drift diode detector (SDD) in single photon counting mode. The effective energy resolution, obtained by convoluting the total instrument energy bandwidth (spreads of the incident and emitted rays) and the $3d_{5/2}$ core-hole width from the $L_{\alpha 1}$ line, was about 3.0 eV, compared to an intrinsic line broadening of about 6.1 eV with an energy-dispersive detector.

The photon energy was calibrated by assigning the maximum of the derivative of the L_3-edge spectrum for elemental Pb to be 13,035.0 eV. The stability in energy (~0.1 eV) was monitored with the Tl_2O_3 reference. The HR-XANES spectra were measured from 12,630 eV to 12,760 eV in continuous scan mode with 0.2 eV step size, and normalized to unity at E = 12,760 eV. A fixed number of 200 scans was collected per sample regardless of the Tl, Fe, and Mn concentrations (1h40 acquisition time). Therefore, the signal-to-noise ratio is proportional on a first order to the Tl concentration (Figure S4a). Data were reduced with the PCA and the LSF programs from beamline 10.3.2 at the Advanced Light Source.[41,71] The accuracy of the fit components (i.e., fraction of Tl(III) and Tl(I)) was estimated to be equal to the variation of their best-fit values when the fit residual (*NSS*) was increased by 20%. The EXAFS spectrum of crust MP23-2 was measured from 12,500 to 13,380 eV in continuous scan mode with 2 eV step size. 1300 scans of 60 s were acquired and averaged to improve statistics. EXAFS data were reduced with the Athena software[69] and fit with Winxas.[72] Theoretical amplitude and phase shift functions were generated with FEFF8.2[73] using the structure of the Tl(III)-TCS DFT complex modeled in this study. The amplitude reduction factor (S_0^2) was fixed to 0.9.

All measurements were performed at a temperature of 10-15 K using a helium flow cryostat and pellets were moved horizontally and vertically after every scan to access unexposed material. No changes in spectral features were noted during the course of data collection that would indicate radiation damage. Marafatto et al.[14] observed that Tl(III) is reduced to Tl(I) at 10 K with a photon flux density of 10^{10}-10^{11} ph/µm^2/sec and is stable at room temperature with a photon density of 0.4-1 × 10^8 ph/µm^2/sec. No radiation damage was observed here at 10-15 K and a photon density of about 10^9 ph/µm^2/sec.

RESULTS

Thallium concentration. The Tl concentration ([Tl]) ranges from 1.5 to 319 ppm in crusts with a mean of 146 ± 93 ppm (n = 17), and ranges from 2 to 112 ppm in nodules with a mean of 19 ± 32 ppm (n = 12) (Table 1). The high variability of [Tl] in the crusts coincides with that reported previously.[2,4] Three crusts from the Pacific Ocean have [Tl] close to, and one above, 300 ppm, which is the highest concentration reported to date. Two out of three of these high-Tl crusts are phosphatized crusts. At least one crust sample from each of the oceans contains >120 ppm Tl, except the Arctic, suggesting that Tl enrichment may not be constrained geographically. The concentration of Tl is also highly variable in nodules, and is on average much lower than that reported previously because the majority of the nodules studied here were buried in marine sediments (Table 1). Nodules at the sediment surface contain 2-112 ppm Tl, those at the subsurface contain 5-15 ppm, and those at >500 cm depth contain 2 ppm. Figure 3a shows [Tl] against the [Mn]/[Fe] weight (wt) ratio. Two data fields can be identified in this figure, one corresponding to the crusts in which [Tl] and [Mn]/[Fe] are correlated (R = 0.92), and the other corresponding to nodules which lack correlation. The positive relationship between [Tl] and [Mn]/[Fe] observed in crusts suggests that Tl is dominantly 3+ and oxidatively scavenged by vernadite, as documented by Peacock and Moon.[9]

Mineralogy. The mineralogy of manganese in FeMn marine oxides is dominated by different types of vernadite (Fe-vernadite, 7 and 10 Å vernadite) and todorokite in proportion that depends on the genetic type of the deposit. Hydrogenetic crusts and nodules formed in contact with oxic seawater contain Fe-vernadite, which consists of birnessite nanosheets exfoliated with feroxyhite (δ-FeOOH) nanoparticles,[17,18,23,74–76] perhaps as a result of the surface catalyzed oxidation of aqueous Fe(II).[77–79] Fe-vernadite has no basal XRD reflection due to the exfoliation of the Mn particles into individual MnO_2 layers.[80] Otherwise a faint 001 reflection is observed when the Mn particles have two or more layers separated by a constant interlayer spacing.[81] The diffraction pattern of Fe-vernadite is characterized by two broadened and asymmetrical *hk*0 peaks at 2.45 Å (100 reflection) and 1.42 Å (110 reflection), also called *hk* bands.[16–18,23] Fe-vernadite starts to dissolve at the early stage of suboxic diagenetic environment and the vernadite component reprecipitates into 10 Å vernadite, which has two hydration layers and a MnO_2-MnO_2 interlayer spacing of 10 Å. The loss of one hydration layer during diagenesis yields 7 Å vernadite. The 10 Å to 7 Å transformation can be performed in the laboratory upon heating to 105-110 °C in air or under vacuum.[23,51,65,66] When diagenesis evolves under more reducing conditions, 10 Å vernadite transforms into todorokite.[23,82–84] Todorokite also has a reflection near 10 Å, but which does not collapse to 7 Å in contrast to 10 Å vernadite. Reduction of insoluble

Fe(III) to soluble Fe(II) under O_2-deficiency increases the Mn/Fe ratio. A Mn/Fe wt ratio of about 2.5 - 3.0 divides purely hydrogenetic precipitates from those that experienced the beginning of early diagenetic transformation.[85–87]

The XRD patterns are shown in Figure S5 and the abundances of the Mn phases are reported in Table 1 together with the Mn/Fe wt ratios. Fe-vernadite is distinctive of all crusts. No 7 Å and 10 Å vernadites were detected in any crust and minor todorokite is observed in one phosphatized crust (MP23-2) out of three. The three phosphatized crusts contain CFA. Evidence for a vernadite-feroxyhite mixing at the nanoscale is provided by Raman spectroscopy. Synthetic δ-MnO_2 has three vibrational modes near 500, 570, and 630 cm^{-1},[88] whereas feroxyhite has a single broad mode in this wavenumber region pointing at 690 cm^{-1} (Figure 4a).[89] The three modes of δ-MnO_2 are also observed in Fe-vernadite, but this spectrum also has a shoulder in the 670-720 cm^{-1} interval attributed to feroxyhite (Figure 4b and S6a). The intensity of the feroxyhite mode varies from crust to crust, being maximum in 74GTV (Figure 4c). Examination of the Raman spectrum for Fe-rich vernadite layers of FeMn nodules from the Mariana Trench shows that the Fe phase is also feroxyhite (Figure S6b).[87] Raman spectroscopy is a surface technique. The penetration depth of the laser source is a complex function of the refraction index, conductivity, and permittivity of the material and varies for example between 0.8-1 μm for silicon and 20-50 nm for germanium at $\lambda = 532$ nm.[90,91] Because the analyzed black spots of Fe-vernadite are close in opacity to Ge, one can estimate that the Raman spectra reflect the composition of the uppermost atomic layers, and therefore confirm the intimate mixing of vernadite and feroxyhite at the nanometer scale.

The mineralogical signature for the hydrogenetic nature of the crusts is backed up by the Mn/Fe wt ratios which range from 0.26 to 2.55 in non-phosphatized crusts and from 1.92 to 3.95 in the three phosphatized crusts. The nodules cover a large range of Mn/Fe wt ratios, extending from 0.41 (hydrogenetic EBS8-6 nodule) up to 30.3 (diagenetic KG1313 nodule). Todorokite occurs in all nodules analyzed here, except in hydrogenetic EBS8-6. Mixed nodules at the sediment surface contain 7 Å and 10 Å vernadite, and minor amounts of todorokite, whereas the buried nodules have exclusively todorokite. The vernadite to todorokite transformation with sediment depth is accompanied by a loss of Tl. Nodules in which only todorokite is detected by XRD have only 2-11 ppm Tl. We shall see below that the remaining Tl pool is dominantly 1+.

Oxidation state of manganese. The Mn K-edge XANES spectra form two groups from visual inspection of their derivatives (Figure S7a). The first group comprises 19 spectra and includes all FeMn crusts (both phosphatized and non-phosphatized), one hydrogenetic nodule (EBS8-6) and one

diagenetic nodule (09KL-44-49cm). Mn is speciated essentially as Fe-vernadite, todorokite being present only in 09KL-44-49cm and a phosphatized crust (MP23-2) (Table 1). The spectra from the first group were averaged to obtain one spectrum representative of the FeMn crusts for use in XANES fitting and further comparisons (Figure 5a). The second group includes all todorokite-containing diagenetic nodules, except 09KL-44-49cm. Their XANES derivatives have a lower amplitude at 6555.7 eV and are shifted to lower energy in the 6547-6562 eV interval (Figure 5b). Comparison of the Mn standards shows that the two spectral features fingerprint higher amounts of Mn(III) and Mn(II) (Figure S7b). The spectra from the second group were not averaged because there is a gradient in the amount of reduced Mn with the sediment depth.

Results from the Combo fits are detailed in Table S4, summarized in Table 2, and two representative fits are shown in Figures 5c and 5d. Mn has an average oxidation state (AOS) of 3.95 ± 0.05 (mean ± accuracy) for the averaged spectrum of all FeMn crusts and a Mn^{3+} fraction lower than 5 %, on average. The oxidation state of Mn in nodules decreases from 3.88 ± 0.08 at the sediment surface (44KG-2) to 3.77 ± 0.08 at 530 cm depth (22KL-1-530cm) and to 3.74 ± 0.07 at 985 cm depth (65SL-985cm). Mn^{2+} makes up <4% of total Mn at all depths, whereas Mn^{3+} increases from 4% at the surface (44KG-2) up to 22% at 985 cm below the surface.

Oxidation state of thallium. *Tl references***.** The Tl L_3-edge XANES spectra arise from the photoelectric ejection of a core $2p_{3/2}$ electron to unoccupied electronic states of s and d symmetry (dipole-allowed $\Delta l = \pm 1$ transitions). Tl(I) has an atomic orbital configuration of $[Xe]6s^24f^{14}5d^{10}6p^0$, and therefore only $2p_{3/2}$ transitions to unbound *n*d ($n \geq 6$) states nominally occur. In contrast to Tl(I), the unoccupied $6s^0$ valence states of Tl(III) make the $2p_{3/2} \rightarrow 6s$ transition possible at low kinetic energy of the photoelectron. Figure 6a shows that the differences between the $TlNO_3$ (Tl(I)) and Tl_2O_3 (Tl(III)) spectra are subtle in the rising edge where electronic transitions to 6s valence states occur.[30] $TlNO_3$ has no structure, in agreement with the nominally occupied 6s states, whereas Tl_2O_3 exhibits a low-edge shoulder at approximately 12,650 eV and a second weaker shoulder in the mid-edge at approximately 12,665 eV. The two features are enhanced at high energy-resolution (Figures 6b), while the $TlNO_3$ low- and mid-edge remain featureless (Figure 6c). Thus, the rising edge of HR-XANES serves as powerful tool to differentiate Tl(I) and Tl(III) by virtue of probing the electronic occupation of the 6s states. In contrast to the low-edge region, the top- and trailing-edge region at 12,670-12,760 eV is sensitive to the local structure of Tl, and therefore is less diagnostic of its oxidation state.

Tl occupies two crystallographic sites in Tl_2O_3, a symmetrical octahedral site (Tl(1)) with 6 O at 2.36 Å, and a distorted octahedral site (Tl(2)) with 2 O at 2.16 Å and 4 O at 2.28 Å (Figure 7).[92] *Ab*

initio FEFF9.6[38] calculation shows that the low-edge peak observed at high energy-resolution in Tl_2O_3 arises from a transition to 6s and 5d states and the mid-edge bump arises from a transition to higher d states (Figure 7a,b). A nominally dipole forbidden weak $2p_{3/2} \rightarrow 5d$ transition is actually observed as a result of the partial mixing of the Tl 6s and 5d states, as shown by valence-band X-ray photoemission and band-structure calculation,[93] and by empty density of states (DOS) calculations (Figure S8). The Tl 6s-5d mixing is higher at the Tl(2) than the Tl(1) site, and the 6s states are less occupied (i.e., the empty density is higher) at the Tl(2) site (Figure S9). These two factors increase the probability of the $2p_{3/2} \rightarrow 6s5d$ transition, which is manifested in the low-edge region as a more intense peak at the Tl(2) site than the Tl(1) site (Figure 7a,b). Therefore, the intensity of the low-edge peak provides a clue to the distribution of the Tl-O distances in a pure Tl(III) compound, and hence of the coordination of Tl (Figure 7c). The low-edge intensity is, however, less diagnostic in mixed-valent Tl(I)-Tl(III) compounds, as Tl(I) has no low-edge structure and, therefore, produces the same effect of decreasing the intensity of the low-edge peak as does the symmetrical Tl(1) site of Tl_2O_3.

FeMn crusts and nodules. The Tl HR-XANES spectra from the marine samples are represented in Figure S9. Investigating all spectra using PCA, we found that only two endmembers were required to account for the variance in the data set (Figure 8a). The first component (PCA) resembles Tl_2O_3 and the second component (PCA2) resembles $TlNO_3$ (Figure 8b). PCA1 has a sharper low-edge peak than Tl_2O_3, which suggests that the Tl(III) site is distorted. The proportions of Tl(III) and Tl(I), as obtained by least-squares fitting with linear combinations of the PCA1 and PCA2 endmember spectra, are given in Tables 1 and S5, and the fits are shown in Figure S9.

The proportion of Tl(III) is >60% in FeMn crusts, and no correlation was observed between the proportion of Tl(III) in the crust and the geographic location or with phosphatization. For nodules, the proportion of Tl(III) is between 0% and 100% (Figure 9, Table S5). Two nodules sampled at the sediment surface have only Tl(III). 21KG-1(n) has 100% Tl(III), [Tl] = 44 ppm, [Mn]/[Fe] = 7.4, Mn AOS = 3.83, and KG1313 has 96 ± 4% Tl(III), [Tl] = 22 ppm, [Mn]/[Fe] = 30.3, Mn AOS = 3.76, and they both contain 10 Å vernadite and todorokite, with minor, residual Fe-vernadite. Although the Mn AOS, [Mn]/[Fe] ratios, and mineralogy indicate that the two nodules were affected by suboxic diagenesis, the O_2-depletion is not reflected in the oxidation state of Tl which is 3+.

The other nodules have <80% Tl(III) and are severely depleted in Tl, with explains the noisy shape of the Tl(I) endmember spectrum calculated by PCA (component PCA2, Figure 8a). A prototypical example is the surface layer of the FeMn nodule from the Baltic Sea (BS-surface), which contains only 2 ppm Tl speciated exclusively as Tl(I) and a Tl/As atomic ratio as low as 0.002 (Figure 2b). The three

deepest buried nodules (≥ 530 cm), which contain only todorokite, 2 ppm Tl, and have 3.74 ± 0.07 ≤ Mn AOS ≤ 3.77 ± 0.08, have 50-69% Tl(I). Overall, the higher percentage of Tl(III) in Fe-vernadite crusts and 10 Å vernadite surface nodules (> 60%) and the higher percentage of Tl(I) in deeply buried todorokite nodules (≥ 50%) are consistent with (1) uptake experiments of Tl on manganates, which showed that Tl(I) is oxidized on phyllomanganates and not on tectomanganates,[9,11] and (2) the monovalent state of Tl in the tunnels of hollandite.[94] There is also experimental evidence that the Tl oxidation is hindered on Mn(III)-rich phyllomanganate. 10 Å vernadite has more Mn(III) than Fe-vernadite (Table 2),[23] and therefore is not expected to have up to 96-100% Tl(III), as observed in KG1313 and 21KG-1(n). We will return to this point when discussing the results.

Bonding environment of Tl(III). The EXAFS spectrum and radial structure function (RSF, Fourier transform) of crust MP23-2 show considerable degrees of similarities with published data for Tl(III)-sorbed δ-MnO_2 (Figure 11).[9,11,12] The RSF exhibits a first peak corresponding to the nearest Tl-O shell, and a double second peak corresponding to the nearest and second-nearest Mn shells from the MnO_2 layer. Best fit results were obtained with 3.6 O at 2.18 Å (σ = 0.084 Å), 2.4 O at 2.33 Å (σ = 0.084 Å), 0.9 Mn at 3.22 Å (σ = 0.10 Å), and 3.1 Mn at 3.66 Å (σ = 0.10Å) (Table S6). The coordination number of Tl was enforced to 6 and the mean displacements of bond lengths (σ) were kept identical for the two O sub-shells and for the two Mn shells to decrease correlation between parameters. This highly constrained fit calculation provides an excellent visual description of the experimental data over the entire data range. Fitting the O shell with a single distance resulted in an average Tl-O bond length of 2.21 Å with a large σ value of 0.12 Å and a fit quality degraded by 27%.

DISCUSSION

Sensitivity of HR-XANES to the oxidation state of Tl. The results underscore the enhanced sensitivity of XANES spectroscopy performed at high-energy resolution for the quantitative determination of the oxidation state of Tl in compositionally complex materials down to the ppm level. The precision on the determination of the fraction of Tl(I) and Tl(III) depends on the data quality and how well the Tl(I) and Tl(III) references used to fit data represent the unknown mixed-valent samples. The precision is between 2% and 6% of total Tl for [Tl] > ~10 ppm, and between 3% and 21% below 10 ppm (Figure S4b). The % error and the fit residual (*NSS* parameter) increase abruptly at low Tl concentration where the signal-to-noise ratio deteriorates rapidly (Figure S4b,c). This is because the total acquisition time was the same for all samples (1h40), not because of an inadequate fit model at low Tl concentration. Error bars can be tightened by increasing the counting time. We conclude that it

is possible with HR-XANES to obtain a precision better than 10% on the oxidation state of Tl in natural FeMn oxides down to the ppm level.

Structure of the Tl(III) surface complex on vernadite. We show that HR-XANES is also sensitive to the coordination of Tl(III). Unequal Tl-O distances in Tl_2O_3 are phenomenologically reflected in a single, strong low-edge peak, whereas this peak is a weak doublet when the Tl-O distances are identical. The single peak shape of all Tl(III)-rich samples suggests that the coordination environment of Tl(III) is asymmetric at the vernadite surface, which EXAFS confirmed with a split of the O coordination shell into two sub-shells at 2.18 Å and 2.33 Å. The ambiguity on the tetrahedral or octahedral coordination of the TCS complex (Figure 1) was addressed by the density functional theory (DFT) following a modeling scheme described previously for the complexation of Ni, Cu, Zn, and Pb on birnessite nanolayers (PBE0/def2-TZVP-ecp, Supplementary Information, SI),[89] and by FEFF calculation of the HR-XANES spectra.

The geometry-optimized Tl(III)-TCS complex bonds the three surface oxygen atoms coordinated to two Mn atoms bordering a layer vacancy (O_{2Mn}) at 2 × 2.19 Å + 2.21 Å in octahedral coordination and at 2.10-2.12 Å in tetrahedral coordination, and bonds the water molecules (O_{2H}) at 3 × 2.29-2.30 Å in the first configuration and 2.17 Å in the second (Figure 1). The bond distances are more unequal in octahedral coordination and the predicted $d(^{VI}Tl\text{-}O)$ values are close to the crystallographic distances for the Tl(2) site of Tl_2O_3 and to the EXAFS distances of 2.18 Å and 2.33 Å. The Tl-O_{2Mn} distances are much shorter than the Tl-O_{2H} distances, as also observed with 3d transition metals.[95–100] The water molecules are oriented such that one H from H_2O forms a H-bond with the nearest O_{3Mn} atom, further stabilizing the octahedral complex.

In keeping with the DFT distances, the FEFF-calculated HR-XANES spectrum for the ^{VI}Tl(III)-TCS complex exhibits a sharp near-edge peak (Figure 10a). This peak is also observed for the ^{VI}Tl(III)-DES complex because the predicted Tl-O distances are distributed from 2.21 Å to 2.36 Å (Figure 10a). In contrast, the more regular coordination of the ^{IV}Tl(III)-TCS complex manifests itself in a blunt near-edge structure unfit to data (Figure 10b). A third result in support of a ^{VI}Tl(III)-TCS complex is the Tl(III)-Mn distance. The octahedral complex has a DFT-calculated $d(^{VI}Tl\text{-}Mn)$ = 3.59-3.65 Å, consistent with the EXAFS distance of 3.66 Å, and the tetrahedral complex has $d(^{IV}Tl\text{-}Mn)$ = 3.46-3.55 Å, inconsistent with the EXAFS distance. Therefore, geometry optimization of the Tl(III) surface complexes on a MnO_2 layer based on DFT, together with EXAFS spectroscopy and FEFF calculation of the HR-XANES spectra for the DFT structure models, demonstrate that Tl(III) is octahedrally coordinated on vernadite. HR-XANES cannot differentiate the ^{VI}Tl(III)-TCS and ^{VI}Tl(III)-DES

surface complexes, in contrast to EXAFS which identified the two complexes on the basis of their distinct Tl-Mn distances equal to 3.66 Å and 3.22 Å, respectively. The EXAFS value of 3.22 Å coincides to within ~0.02Å with the DFT value of 3.19-3.20 Å (Figure 1).

Tl uptake in FeMn crusts and nodules. The linear correlation between [Tl] and [Mn]/[Fe] in FeMn crusts is well explained by the oxidative scavenging of thallium by interlayers of Fe-vernadite (Figure 3a). Then, one would expect the proportion of Tl(III) to be also correlated with [Mn]/[Fe], which is not the case since it varies irregularly between 62% and 100% (Figure 3b, Table 1). Hydrogenetic crusts form in oxidizing environments as supported by the 3.95 ± 0.05 average oxidation state of Mn, regardless if the crust is phosphatized (Table 2). Tl(I) sorption experiment on synthetic vernadite (δ-MnO_2) predicts that all the Tl should be trivalent under these conditions.[9,11] Wick et al.[11] observed that Tl(I) sorbed on Mn(III)-free δ-MnO_2 was totally oxidized to Tl(III) up to a Tl/Mn atomic ratio of ~0.02, whereas only 12% Tl(I) was oxidized at Tl/Mn = 0.0023 on δ-MnO_2 containing 17% Mn(III). The Tl loading in the crusts is 10-fold to 500-fold lower ($0.05 \times 10^{-4} \leq$ Tl/Mn $\leq 2.91 \times 10^{-4}$, Table 1) than in the sorption experiment, which added to the mostly fourvalent state of Mn, is incompatible with several tens of percent Tl(I) in some of the crusts. A case in point is sample 232D-B 0-78, which has 21 ± 3% Tl(I) despite having only 1.5 ppm Tl and a Tl/Mn atomic ratio of 0.05×10^{-4} (Table 1). The incomplete oxidative uptake of Tl(I) in crusts cannot be simply explained by the saturation of redox reactive Mn sites due to a surface excess of Tl nor by the abundance of Mn(III). There are potentially several reasons why some of the Tl(I) is recalcitrant to oxidation in crusts.

Three hypotheses can be advanced to explain the occurrence of Tl(I) in crusts that formed in oxygen-rich environments. One is the high affinity of Tl(I) for phyllosilicates. Tl(I) is a chemical analog to K and can replace it in the interlayer of micaceous clay minerals as does Cs.[101] The Tl(I)-clay association is well documented in soils.[10,11,13,14] This explanation seems unlikely, however, because phyllosilicates were detected by XRD in only two crusts, DS4-003A B08-28 and 122K, out of 17 and both contain little Tl(I). The first crust has 94 ± 5% Tl(III) and the second, which is phosphatized, has 79 ± 3% Tl(III). Another possibility is to consider that Tl(I) is associated with feroxyhite in Fe-vernadite since Tl(I) is not oxidized by Fe oxyhydr(oxides). This second hypothesis is incompatible with the results of Peacock and Moon[9] on the 237KD hydrogenetic crust from the Pacific Ocean. The crust had a concentric growth microstructure with alternating Fe-rich and Mn-rich growth layers and element imaging by X-ray micro-fluorescence showed that Tl occurred in the Mn layers, not in the Fe-rich layers.

Using Tl-XANES and Mn-EXAFS spectroscopy, Peacock and Moon[9] also observed that 58 ± 3% of Tl was monovalent in the Mn layers and that 79 ± 10 % of Mn was speciated as hexagonal birnessite and 21 ± 10% as todorokite. Some of the Tl(I) was assumed to be sorbed on birnessite without oxidation, perhaps because the Mn vacancy sites were capped by other cations, such as trace metals, Mn(III) and possibly Fe(III) from feroxyhite. In contrast to transition metals which sorb above octahedral layer vacancies, K sorbs with high affinity at the surface of the MnO_2 layer above tetrahedral cavities formed by three edge-sharing octahedra (Figure 12). This crystallographic position has been described in well-crystallized birnessite synthesized at high temperature[102,103] and in nanoparticulate birnessite (δ-MnO_2) synthesized at ambient condition by *Pseudomonas putida*.[104] Barium also sorbs on this site in natural vernadite,[66] and the coordination of K and Ba on this site coincides with that in the tunnels of tectomanganates.[105] The DFT geometry-optimized Tl(I)-O and Tl(I)-Mn distances are 2.95-3.10 Å and 3.75-3.95 Å, respectively, much larger than the EXAFS distances (Figure 12). Tl(I) does not occupy the center of the cavity but is shifted in direction of one of the three edge-sharing octahedra, as also observed for K and Ba.[66,102,103,105] The offset in position depends on the layer charge and is larger when one of the three underlying Mn cations is Mn(III).[66] In this case, the Tl(I)-O distance with the Mn(III)-bonded oxygen atom undersaturated by the Jahn-Teller distortion is 2.66 Å and the two other oxygen atoms are at 3.03 Å and 3.28 Å from Tl(I). The Tl(I)-Mn distances are between 3.70 Å and 3.87 Å Therefore, we hypothesize that at least part of Tl(I) is taken up on the Ba site of Fe-vernadite in hydrogenetic crusts. This sorption site is abundant since the 17 crusts contain 1523 ± 558 ppm Ba.

Thallium exhibits pronounced depletion at the onset of diagenesis and is as low as 2 ppm in nodules buried at ≥ 530 cm depth (Figure 3a, Table 1). Almost all Tl is released to pore waters under the reducing conditions that prevail at this depth. Todorokite is the only Mn species detected by XRD and has an average Mn oxidation state of 3.74-3.77 ± 0.07, compared to 3.95 ± 0.05 in crusts (Table 2). From 50% to 69% of Tl is monovalent (Table 1), and is likely taken up by todorokite and/or phyllosilicate. Yet, one third to one half of the Tl pool is trivalent. Because todorokite does not oxidize Tl(I),[9,11] the Tl(III) present in trace amounts may be associated with some residual phyllomanganate (< ~ 2-3 mineral %) that did not transform into todorokite during diagenesis.[23,82] It is unlikely an oxidized porewater species sorbed on todorokite, because Tl(III) species are sparingly soluble and Tl^{3+} is a highly hydrolyzable metal ion.

The identity of the Tl(I) carrier phase is less certain in nodules located at the sediment surface and subsurface. The percentage of Tl(I) varies between 0% (21KG-1(n)) and 100% (BS-surface) and does

not covary with the [Mn]/[Fe] ratio (Figure 3b) nor the AOS of Mn (Table 2). For example, thallium is 96% Tl(III) in KG1313 with a Mn AOS of 3.76 ± 0.07 and is 82% Tl(I) in BS-bulk with a similar Mn AOS of 3.79 ± 0.08 (Figure S3) and in addition the two nodules have practically identical mineralogy (Figure S5). Tl(I) can be hosted by vernadite and todorokite, and also phyllosilicate when present. Nodules found at the sediment surface and subsurface are subject to partial diagenetic alteration, therefore have more chemical and structural inhomogeneity than hydrogenetic crusts and fully altered buried nodules. The large variability in the percentage of Tl(I) reflects this complexity and also the larger-scale geochemical diversity of the depositional settings from the global ocean.

The Baltic Sea nodule which was separated into a bulk sample and the <1mm surface layer scraped off with a knife (representing the most recent precipitate of the last decades) has lowest Tl concentrations of 4 ppm and 2 ppm, respectively, which reflects the very high growth rate of about 20 µm $year^{-1}$ compared to deep-sea nodules.[43] The surface layer is the only sample that has an exclusive Tl redox speciation of +1, with the bulk nodule having the second highest Tl(I) fraction of 82%. This nodule can be considered as the FeMn nodule endmember on the low-oxygen side, as it forms under highly variable redox conditions reflected by a distinct early diagenetic Fe-Mn banding.[106] This is related to the seasonal thermohaline stratification in the western Baltic Sea during summer (June to September), which reduces the oxygen flux from the surface to the bottom water. Enhanced decay of organic matter results in oxygen depletion at the bottom which exposes the nodules to suboxic or even anoxic conditions, preventing further oxide precipitation and potentially even remobilizing part of the precipitate diagenetically. In fall and winter when wind and waves replenish oxygen in the deeper water layers, FeMn oxide growth may resume. Apparently, redox conditions are never sufficiently oxidizing to allow substantial Tl(I) oxidation on the Mn oxide; alternatively, this could also be a kinetic effect because the prevailence of more oxidizing conditions is only a few months.

CONCLUSION

The results provoke a revisitation of the enrichment process of Tl in marine ferromanganese deposits. The scavenging of Tl is not solely an oxidative process but also a highly efficient sorption mechanism of Tl(I), probably on the high affinity K/Ba crystallographic sites to balance the charge deficit created by a Mn(III) for Mn(IV) substitution in the manganate structure.[103] Under this premise, the Tl(I)/Tl(III) ratio depends, among other factors, on the density of the vacancy sites and the Mn(III)/Mn(IV) ratio, and therefore on the defective structure and stoichiometry of the Tl host manganate.

Our findings illuminate significant aspects of thallium crystal chemistry and geochemistry in marine ferromanganese deposits. They also give rise to challenging questions and suggest future research directions. Additional studies will be required to investigate how Tl(I) is oxidized mechanistically to Tl(III) by Mn(IV) on layered manganese oxides. EXAFS spectroscopy showed that Tl(III) is bonded to the edge and vacancy sites of Fe-vernadite, but only one sample was analyzed (MP23-2) with a rather high Tl concentration (283 ppm). Questions remain as to which of the two sites is most reactive and which dominates the partitioning of Tl at low concentration. The sorption sites of Tl(I) on (Fe)-vernadite and todorokite also remain unknown. Perhaps Tl(I) is substituted for K^+ and/or Ba^{2+} in the interlayers of (Fe)-vernadite and in the tunnels of todorokite, but this hypothesis needs to be tested. All these important crystal chemical questions underlying the geochemical partitioning of Tl between seawater and FeMn crusts and nodules, on the one hand, and in coexisting manganese minerals, on the other hand, are now leading to investigations in natural marine deposits by HR-XANES and EXAFS spectroscopy down to the ppm level.

ASSOCIATED CONTENT

Supporting Information

The Supporting Information is available free of charge on the ACS Publications website at DOI:

DFT method, supplementary figures S1-S9 and tables S1, S3, S5, S6 (PDF)

Supplementary tables S2 and S4, and Cartesian coordinates of the surface complexes (xlsx)

AUTHOR INFORMATION

Corresponding Authors

E-mail: alain.manceau@univ-grenoble-alpes.fr; a.koschinsky@jacobs-university.de

ORCID

Blanka Detlefs : 0000-0002-9768-647X

Pieter Glatzel : 0000-0001-6532-8144

James Hein: 0000-0002-5321-899X

Andrea Koschinsky: 0000-0002-9224-0663

Alain Manceau: 0000-0003-0845-611X

Kira Mizell: 0000-0002-5066-787X

Alexandre Simionovici: 0000-0001-5349-6482

Notes

The authors declare no competing financial interests.

ACKNOWLEDGMENTS

Thomas Kuhn is acknowledged for providing sample SO92 74GTV and information on it, Wouter van Beek, BM31, is acknowleged for support with the Mn-XANES measurements, Alexander Sobolev is acknowleged for providing access to the RAMAN microscope at ISTerre, and four anonymous reviewers are acknowledged for constructive comments on the manuscript. This equipment has been funded by ERC Synergy 856555 MEET project and by Isere Department, France. Support was provided to A. Simionovici by the Institut Universitaire de France.

REFERENCES

(1) Koschinsky, A.; Hein, J. R. Uptake of Elements from Seawater by Ferromanganese Crusts: Solid-Phase Associations and Seawater Speciation. *Mar. Geol.* **2003**, *198*, 331-351.

(2) Rehkamper, M.; Frank, M.; Hein, J. R.; Halliday, A. Cenozoic Marine Geochemistry of Thallium Deduced from Isotopic Studies of Ferromanganese Crusts and Pelagic Sediments. *Earth Planet. Sci. Lett.* **2004**, *219* (1–2), 77–91.

(3) Rehkamper, M.; Nielsen, S. G. The Mass Balance of Dissolved Thallium in the Oceans. *Mar. Chem.* **2004**, *85*, 125–139.

(4) Hein, J. R.; Mizell, K.; Koschinsky, A.; Conrad, T. A. Deep-Ocean Mineral Deposits as a Source of Critical Metals for High- and Green-Technology Applications: Comparison with Land-Based Resources. *Ore Geol. Rev.* **2013**, *51*, 1–14.

(5) Hein, J. R.; Koschinsky, A. Deep-Ocean Ferromanganese Crusts and Nodules. In *Treatrise on Geochemistry*; Holland, H. D., Turekian, K. K., Eds.; Oxford: Elsevier, 2014; Vol. 1–16, pp 273-291.

(6) Nielsen, S. G.; Mar-Gerrison, S.; Gannoun, A.; LaRowe, D.; Klemm, V.; Halliday, A. N.; Burton, K. W.; Hein, J. R. Thallium Isotope Evidence for a Permanent Increase in Marine Organic Carbon Export in the Early Eocene. *Earth Planet. Sci. Lett.* **2009**, *278* (3–4), 297–307.

(7) Karbowska, B. Presence of Thallium in the Environment: Sources of Contaminations, Distribution and Monitoring Methods. *Environ. Monit. Assess.* **2016**, *188*, n° 640.

(8) Bidoglio, G.; Gibson, P. N.; O'Gorman, M.; Roberts, K. J. X-Ray Absorption Spectroscopy Investigation of Surface Redox Transformations of Thallium and Chromium on Colloidal Mineral Oxides. *Geochim. Cosmochim. Acta* **1993**, *57*, 2389–2394.

(9) Peacock, C. L.; Moon, E. M. Oxidative Scavenging of Thallium by Birnessite: Explanation for Thallium Enrichment and Stable Isotope Fractionation in Marine Ferromanganese Precipitates. *Geochim. Cosmochim. Acta* **2012**, *84*, 297–313.

(10) Voegelin, A.; Pfenninger, N.; Petrikis, J.; Majzlan, J.; Plotze, M.; Senn, A. C.; Mangold, S.; Steininger, R.; Gottlicher, J. Thallium Speciation and Extractability in a Thallium- and Arsenic-Rich Soil Developed from Mineralized Carbonate Rock. *Environ. Sci. Technol.* **2015**, *49*, 5390–5398.

(11) Wick, S.; Pena, J.; Voegelin, A. Thallium Sorption onto Manganese Oxides. *Environ. Sci. Technol.* **2019**, *53*, 13168–13178.

(12) Cruz-Hernandez, Y.; Villalobos, M.; Marcus, M. A.; Pi-Puig, T.; Zanella, R.; Martinez-Villegas, N. Tl(I) Sorption Behavior on Birnessite and Its Implications for Mineral Structural Changes. *Geochim. Cosmochim. Acta* **2019**, *248*, 356–369.

(13) Wick, S.; Baeyens, B.; Fernandes, M. M.; Gottlicher, J.; Fischer, M.; Pfenninger, N.; Plotze, M.; Voegelin, A. Thallium Sorption and Speciation in Soils: Role of Micaceous Clay Minerals and Manganese Oxides. *Geochim. Cosmichim. Acta* **2020**, *288*, 83–100.

(14) Marafatto, F. F.; Dähn, R.; Grolimund, D.; Göttlicher, J.; Voegelin, A. Thallium Sorption by Soil Manganese Oxides: Insights from Synchrotron X-Ray Micro-Analyses on a Naturally Thallium-Rich Soil. *Geochim. Cosmochim. Acta* **2021**, *302*, 193–208.

(15) Drits, V. A.; Silvester, E.; Gorshkov, A. I.; Manceau, A. Structure of Synthetic Monoclinic Na-Rich Birnessite and Hexagonal Birnessite. Part 1. Results from X-Ray Diffraction and Selected Area Electron Diffraction. *Am. Miner.* **1997**, *82*, 946–961.

(16) Ostwald, J. Ferruginous Vernadite in an Indian Ocean Ferromanganese Nodule. *Geol. Mag.* **1984**, *121*, 483–488.

(17) Manceau, A.; Combes, J. M. Structure of Mn and Fe Oxides and Oxyhydroxides: A Topological Approach by EXAFS. *Phys. Chem. Miner.* **1988**, *15*, 283–295.

(18) Manceau, A.; Gorshkov, A. I.; Drits, V. A. Structural Chemistry of Mn, Fe, Co, and Ni in Mn Hydrous Oxides. II. Information from EXAFS Spectroscopy, Electron and X-Ray Diffraction. *Am. Miner.* **1992**, *77*, 1144–1157.

(19) Hochella, M. F.; Kasama, T.; Putnis, A.; Putnis, C. V.; Moore, J. N. Environmentally Important, Poorly Crystalline Fe/Mn Hydrous Oxides: Ferrihydrite and a Possibly New Vernadite-like Mineral from the Clark Fork River Superfund Complex. *Am. Miner.* **2005**, *90*, 718–724.

(20) Lee, S.; Xu, H.; Xu, W.; Sun, X. The Structure and Crystal Chemistry of Vernadite in Ferromanganese Crusts. *Acta Cryst. B* **2019**, *75*, 591–598.

(21) Post, J. E.; Bish, D. L. Rietveld Refinement of the Todorokite Structure. *Am. Miner.* **1988**, *73*, 861-869.

(22) Post, J. E.; Heaney, P. J.; Hanson, J. Synchrotron X-Ray Diffraction of the Structure and Dehydration Behavior of Todorokite. *Am. Miner.* **2003**, *88*, 142–150.

(23) Manceau, A.; Lanson, M.; Takahashi, Y. Mineralogy and Crystal Chemistry of Mn, Fe, Co, Ni, and Cu in a Deep-Sea Pacific Polymetallic Nodule. *Am. Miner.* **2014**, *99*, 2068–2083.

(24) Lee, P. A.; Citrin, P. H.; Eisenberger, P.; Kincaid, B. M. Extended X-Ray Absorption Fine Structure—Its Strengths and Limitations as a Structural Tool. *Rev. Mod. Phys.* **1981**, *53*, 769–800.

(25) Rovezzi, M.; Lapras, C.; Manceau, A.; Glatzel, P.; Verbeni, R. High Energy-Resolution x-Ray Spectroscopy at Ultra-High Dilution with Spherically Bent Crystal Analyzers of 0.5 m Radius. *Rev. Sci. Instr.* **2017**, *88*, 013108.

(26) Glatzel, P.; de Groot, F. M. F.; Manoilova, O.; Grandjean, D.; Weckhuysen, B. M. Range-Extended EXAFS at the L Edge of Rare Earths Using High-Energy-Resolution Fluorescence Detection: A Study of La in LaOCl. *Phys. Rev. B* **2005**, *72*, n° 014117.

(27) Campbell, J. L.; Papp, T. Widths of the Atomic K-N7 Levels. *Atom. Data and Nucl. Data* **2001**, *77*, 1–56.

(28) Hämäläinen, K.; Siddons, D. P.; Hastings, J. B.; Berman, L. E. Elimination of the Inner-Shell Lifetime Broadening in X-Ray-Absorption Spectroscopy. *Phys. Rev. Lett.* **1991**, *67*, 2850–2853.

(29) Atkins, A. L.; Shaw, S.; Peacock, C. L. Release of Ni from Birnessite during Transformation of Birnessite to Todorokite: Implications for Ni Cycling in Marine Sediments. *Geochim. Cosmochim. Acta* **2016**, *189*, 158–183.

(30) George, L. L.; Biagionia, C.; Leporeb, G. O.; Lacalamita, M.; Agrosìc, G.; Capitanid, G. C.; Bonaccorsia, E.; d'Acapito, F. The Speciation of Thallium in (Tl,Sb,As)-Rich Pyrite. *Ore Geol. Rev.* **2019**, *107*, 364–380.

(31) Glatzel, P.; Sikora, M.; Smolentsev, G.; Fernandez-Garcia, M. Hard X-Ray Photon-in Photon-out Spectroscopy. *Catal. Today* **2009**, *145*, 294–299.

(32) Le Pape, P.; Blanchard, M.; Juhin, A.; Rueff, J. P.; Ducher, M.; Morin, G.; Cabaret, D. Local Environment of Arsenic in Sulfide Minerals: Insights from High-Resolution X-Ray Spectroscopies, and First-Principles Calculations at the As K-Edge. *J. Anal. Atom. Spec.* **2018**, *33*, 2070–2082.

(33) Merkulova, M.; Mathon, O.; Glatzel, P.; Batanova, V.; Marion, P.; Boiron, M. C.; Manceau, A. Revealing the Chemical Form of "Invisible" Gold in Natural Arsenian Pyrite and Arsenopyrite with High Energy-Resolution X-Ray Absorption Spectroscopy. *ACS Earth Space Chem.* **2019**, *3*, 1905–1914.

(34) Manceau, A.; Merkulova, M.; Mathon, O.; Glatzel, P.; Murdzek, M.; Batanova, V.; Simionovici, A.; Steinmann, S. N.; Paktunc, D. The Mode of Incorporation of As(-I) and Se(-I) in Natural Pyrite Revisited. *ACS Earth Space Chem.* **2020**, *4*, 379–390.

(35) Filimonova, O. N.; Tagirov, B. R.; Trigub, A. L.; Nickolsky, M. S.; Rovezzi, M.; Belogub, E. V.; Reukov, V. L.; Vikentyev, I. V. The State of Au and As in Pyrite Studied by X-Ray Absorption Spectroscopy of Natural Minerals and Synthetic Phases. *Ore Geol. Rev.* **2020**, *121*, n° 103475.

(36) Le Pape, P.; Stetten, L.; Hunault, M.; Mangeret, A.; Brest, J.; Boulliard, J. C.; Morin, G. HERFD-XANES Spectroscopy at the U M_4-Edge Applied to the Analysis of U Oxidation State in a Heavily Contaminated Wetland Soil. *Appl. Geochem.* **2020**, *122*.

(37) Dublet, G.; Juillot, F.; Brest, J.; Noel, V.; Fritsch, E.; Proux, O.; Olivi, L.; Ploquin, F.; Morin, G. Vertical Changes of the Co and Mn Speciation along a Lateritic Regolith Developed on Peridotites (New Caledonia). *Geochim. Cosmochim. Acta* **2017**, *217*, 1–15.

(38) Rehr, J. J.; Kas, J. J.; Vila, F. D.; Prange, M. P.; Jorissen, K. Parameter-Free Calculations of X-Ray Spectra with FEFF9. *Phys. Chem. Chem. Phys.* **2010**, *12*, 5503–5513.

(39) Ressler, T.; Wong, J.; Roos, J.; Smith, I. Quantitative Speciation of Mn-Bearing Particulates Emitted from Autos Burning (Methylcyclopentadienyl)Manganese Tricarbonyl-Added Gasolines Using XANES Spectroscopy. *Environ. Sci. Technol.* **2000**, *34*, 950–958.

(40) Rossberg, A.; Reich, T.; Bernhard, G. Complexation of Uranium(VI) with Protocatechuic Acid-Application of Iterative Transformation Factor Analysis to EXAFS Spectroscopy. *Anal. Bioanal. Chem.* **2003**, *376*, 631–638.

(41) Manceau, A.; Marcus, M. A.; Tamura, N. Quantitative Speciation of Heavy Metals in Soils and Sediments by Synchrotron X-Ray Techniques. In *Applications of Synchrotron Radiation in Low-Temperature Geochemistry and Environmental Science*; Fenter, P. A., Rivers, M. L., Sturchio, N. C., Sutton, S. R., Eds.; Reviews in Mineralogy and Geochemistry; Mineralogical Society of America: Washington, DC, 2002; Vol. 49, pp 341–428.

(42) Manceau, A.; Marcus, M.; Lenoir, T. Estimating the Number of Pure Chemical Components in a Mixture by X-Ray Absorption Spectroscopy. *J. Synchrotron Radiat.* **2014**, *21*, 1140–1147.

(43) Hlawatsch, S.; Neumann, T.; van den Berg, C. M. G.; Kersten, M.; Harff, J.; Suess, E. Fast-Growing, Shallow-Water Ferro-Manganese Nodules from the Western Baltic Sea: Origin and Modes of Trace Element Incorporation. *Mar. Geol.* **2002**, *182*, 373–387.

(44) Koschinsky, A.; Halbach, P. Sequential Leaching of Marine Ferromanganese Precipitates: Genetic Implications. *Geochim. Cosmochim. Acta* **1995**, *59*, 5113–5132.

(45) Bau, M.; Koschinsky, A.; Dulski, P.; Hein, J. R. Comparison of the Partitioning Behaviours of Yttrium, Rare Earth Elements, and Titanium between Hydrogenetic Marine Ferromanganese Crusts and Seawater. *Geochim. Cosmichim. Acta* **1996**, *60*, 1709–1725.

(46) Kuhn, T.; Bau, M.; Blum, N.; Halbach, P. Origin of Negative Ce Anomalies in Mixed Hydrothermal-Hydrogenetic Fe–Mn Crusts from the Central Indian Ridge. *Earth Planet. Sci. Lett.* **1998**, *163*, 207–220.

(47) Schmidt, K.; Blau, M.; Hein, J. R.; Koschinsky, A. Fractionation of the Geochemical Twins Zr-Hf and Nb-Ta during Scavenging from Seawater by Hydrogenetic Ferromanganese Crusts. *Geochim. Cosmochim. Acta* **2014**, *140*, 468–487.

(48) Wegorzewski, A. V.; Kuhn, T. The Influence of Suboxic Diagenesis on the Formation of Manganese Nodules in the Clarion Clipperton Nodule Belt of the Pacific Ocean. *Mar. Geol.* **2014**.

(49) Wegorzewski, A. V.; Kuhn, T.; Dohrmann, R.; Wirth, R.; Grangeon, S. Mineralogical Characterization of Individual Growth Structures of Mn-Nodules with Different Ni+Cu Content from Central Pacific Ocean. *Am. Miner.* **2015**, *110*, 2497–2508.

(50) Koschinsky, A.; Hein, J. R.; Kraemer, D.; Foster, A. L.; Kuhn, T.; Halbach, P. Platinum Enrichment and Phase Associations in Marine Ferromanganese Crusts and Nodules Based on a Multi-Method Approach. *Chem. Geol.* **2020**, *539*, n° 119426.

(51) Wegorzewski, A. V.; Grangeon, S.; Webb, S. M.; Heller, C.; Kuhn, T. Mineralogical Transformations in Polymetallic Nodules and the Change of Ni, Cu and Co Crystal-Chemistry upon Burial in Sediments. *Geochim. Cosmochim. Acta* **2020**, *282*, 19–37.

(52) Hein, J. R.; Koschinsky, A.; Kuhn, T. Deep- Ocean Polymetallic Nodules as a Resource for Critical Materials. *Nat. Rev. Earth Environ.* **2020**, *1*, 159–169.

(53) Koschinsky, A.; Stascheit, A.; Bau, M.; Halbach, P. Effects of Phosphatization on the Geochemical and Mineralogical Composition of Marine Ferromanganese Crusts. *Geochim. Cosmochim. Acta.* **1997**, *61*, 4079–4094.

(54) Koschinsky, A.; VanGerven, M.; Halbach, P. First Investigations of Massive Ferromanganese Crusts in the NE Atlantic in Comparison with Hydrogenetic Pacific Occurrences. *Mar. Georesources Geotechnol.* **1995**, *13*, 375–391.

(55) Koschinsky, A.; Halbach, P.; Hein, J. R.; Mangini, A. Ferromanganese Crusts as Indicators for Paleoceanographic Events in the NE Atlantic. *Geol. Rdsch.* **1996**, *85*, 567–576.

(56) Yeo, I. A.; Howarth, S. A.; Spearman, J.; Cooper, A.; Crossouard, N.; Taylor, J.; Turnbull, M.; Murton, B. J. Distribution of and Hydrographic Controls on Ferromanganese Crusts: Tropic Seamount, Atlantic. *Ore Geol. Rev.* **2019**, *114*, 11.

(57) Josso, P.; Rushton, J.; Lusty, P.; Matthews, A.; Chenery, S.; Holwell, D.; Kemp, S. J.; Murton, B. Late Cretaceous and Cenozoic Paleoceanography from North-East Atlantic Ferromanganese Crust Microstratigraphy. *Mar. Geol.* **2020**, *422*, n° 106122.

(58) Hein, J. R.; Konstantinova, N.; Mikesell, M.; Mizell, K.; Fitzsimmons, J. N.; Lam, P. J.; Jensen, L. T.; Xiang, Y.; Gartman, A.; Cherkashov, G.; Hutchinson, D. R.; Till, C. P. Arctic Deep Water Ferromanganese-Oxide Deposits Reflect the Unique Characteristics of the Arctic Ocean. *Geochem. Geophys. Geosys.* **2017**, *18*, 3771–3800.

(59) Hlawatsch, S.; Kersten, M.; Garbe-Schönberg, C. D.; Lechtenberg, F.; Manceau, A.; Tamura, N.; Kulik, D. A.; Harff, J.; Suess, E. Trace Metal Fluxes to Ferromanganese Nodules from the Western Baltic Sea as a Record for Long-Term Environmental Changes. *Chem. Geol.* **2002**, *182*, 697–710.

(60) von Stackelberg, U. Manganese Nodules of the Peru Basin. In *Handbook of Marine Mineral Deposits*; Cronan, D., Ed.; Taylor & Francis Group: Boca Raton, 2017; p 42.

(61) Halbach, P.; Friendrich, G.; von Stackelberg, U. *The Manganese Nodule Belt of the Pacific Ocean*; Enke: Stuttgart, 1988.

(62) Hein, J. R.; Conrad, T.; Mizell, K.; Banakar, V. K.; Frey, F. A.; Sager, W. W. Controls on Ferromanganese Crust Composition and Reconnaissance Resource Potential, Ninetyeast Ridge, Indian Ocean. *Deep Sea Res. Part I Oceanogr. Res. Pap.* **2016**, *110*, 1–19.

(63) Dulski, P. Reference Materials for Geochemical Studies: New Analytical Data by ICPMS and Critical Discussion of Reference Values. *Geostand. Newslett.* **2001**, *25*, 87–125.

(64) Alexander, B. W. *Trace Element Analyses in Geological Materials Using Low Resolution Inductively Coupled Plasma Mass Spectrometry (ICPMS)*; School of Engineering and Science; Jacobs University, Bremen, 2008.

(65) Usui, A.; Mita, N. Geochemistry and Mineralogy of a Modern Buserite Deposit from a Hot Spring in Hokkaido, Japan. *Clays Clay Miner.* **1995**, *43*, 116–127.

(66) Manceau, A.; Lanson, M.; Geoffroy, N. Natural Speciation of Ni, Zn, Ba and As in Ferromanganese Coatings on Quartz Using X-Ray Fluorescence, Absorption, and Diffraction. *Geochim. Cosmochim. Acta* **2007**, *71*, 95–128.

(67) van Beek, W.; Emerich, H.; Chernyshov, D.; Dyadkin, V.; Wiker, G.; Dmitriev, V. SNBL'S BM31 at ESRF beyond 2020 - Combined XRD-PDF-XAS. *Acta Cryst. A* **2019**, *75*, 677–677.

(68) Kraft, S.; Stümpel, J.; Becker, P.; Kuetgens, U. High Resolution X-Ray Absorption Spectroscopy with Absolute Energy Calibration for the Determination of Absorption Edge Energies. *Rev. Sci. Instrum.* **1996**, *67*, 681–687.

(69) Ravel, B.; Newville, M. ATHENA, ARTEMIS, HEPHAESTUS: Data Analysis for X-Ray Absorption Spectroscopy Using IFEFFIT. *J. Synchrotron Radiat.* **2005**, *12*, 537–541.

(70) Manceau, A.; Marcus, M. A.; Grangeon, S. Determination of Mn Valence States in Mixed-Valent Manganates by XANES Spectroscopy. *Am. Miner.* **2012**, *97*, 816–827.

(71) Marcus, M. A.; MacDowell, A. A.; Celestre, R.; Manceau, A.; Miller, T.; Padmore, H. A.; Sublett, R. E. Beamline 10.3.2 at ALS: A Hard X-Ray Microprobe for Environmental and Materials Sciences. *J. Synchrotron Radiat.* **2004**, *11*, 239–247.

(72) Ressler, T. WinXAS: A Program for X-Ray Absorption Spectroscopy Data Analysis under MS-Windows. *J. Synchrotron Radiat.* **1998**, *5*, 118–122.

(73) Ankudinov, A. L.; Rehr, J. J. Relativistic Calculations of Spin-Dependent X-Ray-Absorption Spectra. *Phys. Rev. B* **1997**, *56*, 1712–1716.

(74) Burns, R. G.; Burns, V. M. Mechanism for Nucleation and Growth of Manganese Nodules. *Nature* **1975**, *255*, 130–131.

(75) Golden, D. C.; Chen, C. C.; Dixon, J. B. Synthesis of Todorokite. *Science* **1986**, *231*, 717–719.

(76) Varentsov, I. M.; Drits, V. A.; Gorshkov, A. I.; Sivtsov, A. V.; Sakharov, B. A. Me-Fe Oxyhydroxide Crusts from Krylov Seamount (Eastern Atlantic): Mineralogy, Geochemistry and Genesis. *Mar. Geol.* **1991**, *96*, 53–70.

(77) Krishnamurti, G. S. R.; Huang, P. M. The Catalytic Role of Birnessite in the Transformation of Iron. *Can. J. Soil Sci.* **1987**, *67*, 533–543.

(78) Postma, D. Concentration of Mn and Separation from Fe in Sediments-I. Kinetics and Stoichiometry of the Reaction between Biiessite and Dissolved Fe(H) at 10°C. *Geochim. Cosm. Acta* **1985**, *49*, 1023–1033.

(79) Gao, T.; Shen, Y.; Jia, Z.; Qiu, G.; Liu, F.; Zhang, Y.; Feng, X.; Cai, C. Interaction Mechanisms and Kinetics of Ferrous Ion and Hexagonal Birnessite in Aqueous Systems. *Geochem. Trans.* **2015**, *16*, n° 16.

(80) Song, M. S.; Lee, K. M.; Lee, Y. R.; Kim, I. Y.; Kim, T. W.; Gunjakar, J. L.; Hwang, S. J. Porously Assembled 2D Nanosheets of Alkali Metal Manganese Oxides with Highly Reversible Pseudocapacitance Behaviors. *J. Phys. Chem. C* **2010**, *114*, 22134–22140.

(81) Manceau, A.; Marcus, M. A.; Grangeon, S.; Lanson, M.; Lanson, B.; Gaillot, A. C.; Skanthakumar, S.; Soderholm, L. Short-Range and Long-Range Order of Phyllomanganate Nanoparticles Determined Using High Energy X-Ray Scattering. *J. Appl. Crystallogr.* **2013**, *46*, 193–209.

(82) Bodei, S.; Manceau, A.; Geoffroy, N.; Baronnet, A.; Buatier, M. Formation of Todorokite from Vernadite in Ni-Rich Hemipelagic Sediments. *Geochim. Cosmochim. Acta*. **2007**, *71*, 5698–5716.

(83) Wu, Z. K.; Peacock, C. L.; Lanson, B.; Yin, H.; Zheng, L. R.; Chen, Z. J.; Tan, W. F.; Qiu, G. H.; Liu, F.; Feng, X. H. Transformation of Co-Containing Birnessite to Todorokite: Effect of Co on the Transformation and Implications for Co Mobility. *Geochim. Cosmochim. Acta* **2019**, *246*, 21–40.

(84) Liang, X. R.; Post, J. E.; Lanson, B.; Wang, X. M.; Zhu, M. Q.; Liu, F.; Tan, W. F.; Feng, X. H.; Zhu, G. M.; Zhang, X.; De Yoreo, J. J. Coupled Morphological and Structural Evolution of δ-MnO_2 to α-MnO_2 through Multistage Oriented Assembly Processes: The Role of Mn(III). *Environ. Sci.-Nano* **2020**, *7*, 238–249.

(85) Halbach, P.; Scherhag, C.; Hebisch, U.; Marchig, V. Geochemical and Mineralogical Control of Different Genetic Types of Deep-Sea Nodules from the Pacific Ocean. *Miner. Deposita* **1981**, *16*, 59–64.

(86) Li, D.; Fu, Y.; Sun, X. Critical Metal Enrichment Mechanism of Deep-Sea Hydrogenetic Nodules: Insights from Mineralogy and Element Mobility. *Ore Geol. Rev.* **2019**.

(87) Li, J. W.; Li, L.; Bai, S. J.; Chen, S.; Xu, H. C.; Ta, K. W.; Qu, Y. G.; Wang, Y. G.; Yao, H. Q.; Dong, Y. H.; Dasgupta, S.; Du, M. R.; Liu, S. Q.; Lin, F. Y.; Peng, X. T. Geochemical and Molecular Characteristics of Ferromanganese Deposits and Surrounding Sediments in the Mariana Trench: An Implication for the Geochemical Mn Cycle in Sedimentary Environments of the Trench Zone. *Geochim. Cosmochim. Acta* **2021**, *310*, 155–168.

(88) Post, J. E.; McKeown, D. A.; Heaney, P. J. Raman Spectroscopy Study of Manganese Oxides: Layer Structures. *Am. Miner.* **2021**, *106*, 351–366.

(89) Bellot-Gurlet, L.; Neff, D.; Reguer, S.; Monnier, J.; Saheb, M.; Dillmann, P. Raman Studies of Corrosion Layers Formed on Archaeological Irons in Various Media. *J. Nano Res.* **2009**, *8*, 147–156.

(90) Shur, M. S. *Physics of Semiconductor Devices*; Englewood Cliffs, N.J., U.S.A., 1990.

(91) Horiba. Strain Measurements of a Si Cap Layer Deposited on a SiGe Substrate Determination of Ge Content. https://www.horiba.com/fileadmin/uploads/Scientific/Documents/Raman/Semiconductors01.pdf.

(92) Gomis, O.; Santamaria-Perez, D.; Ruiz-Fuertes, J.; Sans, J. A.; Vilaplana, R.; Ortiz, H. M.; Garcia-Domene, B.; Manjon, F. J.; Errandonea, D.; Rodriguez-Hernandez, P.; Munoz, A.; Mollar, M. High-Pressure Structural and Elastic Properties of Tl_2O_3. *J. Appl. Phys.* **2014**, *116*, n° 133521.

(93) Glans, P. A.; Learmonth, T.; Smith, K. E.; Guo, J.; Walsh, A.; Watson, G. W.; Terzi, F.; Egdell, R. G. Experimental and Theoretical Study of the Electronic Structure of HgO and Tl_2O_3. *Phys. Rev. B* **2005**, *71*, 235109.

(94) Gołębiowska, B.; Pieczka, A.; Zubko, M.; Voegelin, A.; Göttlicher, J.; Rzepa, G. Thalliomelane, $TlMn^{4+}_{7.5}\ Cu^{2+}_{0.5}\ O_{16}$, a New Member of the Coronadite Group from the Preglacial Oxidation Zone at Zalas, Southern Poland. *Am. Miner.* **2021**, in press.

(95) Post, J. E.; Appleman, D. E. Chalcophanite, $ZnMn_3O_7{:}3H_2O$: New Crystal-Structure Determination. *Am. Miner.* **1988**, *73*, 1401–1404.

(96) Manceau, A.; Lanson, B.; Drits, V. A. Structure of Heavy Metal Sorbed Birnessite. Part III. Results from Powder and Polarized Extended X-Ray Absorption Fine Structure Spectroscopy. *Geochim. Cosmochim. Acta.* **2002**, *66*, 2639–2663.

(97) Toner, B.; Manceau, A.; Webb, S. M.; Sposito, G. Zinc Sorption to Biogenic Hexagonal-Birnessite Particles within a Hydrated Bacterial Biofilm. *Geochim. Cosmochim. Acta.* **2006**, *70*, 27–43.

(98) Kwon, K. D.; Refson, K.; Sposito, G. Zinc Surface Complexes on Birnessite: A Density Functional Theory Study. *Geochim. Cosmochim. Acta* **2009**, *73*, 1273–1284.

(99) Kwon, K. D.; Refson, K.; Sposito, G. Understanding the Trends in Transition Metal Sorption by Vacancy Sites in Birnessite. *Geochim. Cosmochim. Acta* **2013**, *101*, 222–232.

(100) Manceau, A.; Steinmann, S. N. Nature of High- and Low-Affinity Metal Surface Sites on Birnessite Nanosheets. *ACS Earth Space Chem.* **2021**, *5*, 66–76.

(101) Wick, S.; Baeyens, B.; Fernandes, M. M.; Voegelin, A. Thallium Adsorption onto Illite. *Environ. Sci. Technol.* **2018**, *52*, 571–580.

(102) Gaillot, A. C.; Flot, D.; Drits, V. A.; Burghammer, M.; Manceau, A.; Lanson, B. Structure of Synthetic K-Rich Birnessites Obtained by High-Temperature Decomposition of $KMnO_4$. I. Two-Layer Polytype from a 800°C Experiment. *Chem. Mater.* **2003**, *15*, 4666–4678.

(103) Gaillot, A. C.; Drits, V. A.; Manceau, A.; Lanson, B. Structure of the Synthetic K-Rich Phyllomanganate Birnessite Obtained by High-Temperature Decomposition of $KMnO_4$: Substructures of K-Rich Birnessite from 1000°C Experiment. *Micropor. Mesopor. Mat.* **2007**, *98*, 267–282.

(104) Villalobos, M.; Lanson, B.; Manceau, A.; Toner, B.; Sposito, G. Structural Model for the Biogenic Mn Oxide Produced by *Pseudomonas Putida*. *Am. Miner.* **2006**, *91*, 489–502.

(105) Manceau, A.; Kersten, M.; Marcus, M. A.; Geoffroy, N.; Granina, L. Ba and Ni Speciation in a Nodule of Binary Mn Oxide Phase Composition from Lake Baikal. *Geochim. Cosmochim. Acta.* **2007**, *71*, 1967–1981.

(106) Glasby, G. P.; Emelyanov, E. M.; Zhamoida, V. A.; Baturin, G. N.; Leipe, T.; Bahlo, R.; Bonacker, P. Environments of Formation of Ferromanganese Concretions in the Baltic Sea: A Critical Review. In *Manganese Mineralization: Geochemistry and Mineralogy of Terrestrial and Marine Deposits*; Nicholson, K., Hein, J. R., Buhn, B., Dasgupta, S., Eds.; Geol. Soc. Spec. Publ., 1997; Vol. 119, pp 213–237.

(107) Sole, V. A.; Papillon, E.; Cotte, M.; Walter, P.; Susini, J. A Multiplatform Code for the Analysis of Energy-Dispersive X-Ray Fluorescence Spectra. *Spectrochim. Acta, B* **2007**, *62*, 63–68.

FIGURE LEGENDS

Figure 1. Geometry-optimized surface complexes of Tl(III) on a phyllomanganate layer. (a) Tridentate corner-sharing (TCS) octahedral complex over a Mn(IV) layer vacancy. (b) Double edge-sharing (DES) octahedral complex on a layer edge. (c) TCS tetrahedral complex over a vacancy site. PBE0/def2-TZVP-ecp modeling scheme (SI). Mn octahedron = gray; Tl(III) octahedron = dark red; oxygen = red, proton = gray.

Figure 2. X-ray fluorescence spectra in the energy range of the Tl $L_{\alpha 1}$ fluorescence line measured with an energy dispersive detector and fit with PyMCA.[107] (a,b) Spectra of crust MP-23-2 and the surface layer of the Baltic Sea nodule[43,59] measured at 13,000 eV. (c) Spectrum of crust MP23-2 measured at 13,500 eV, above the Pb L_3-edge (13,035 eV). The Tl concentrations and the Tl/As atomic ratios are 283 ppm and 0.69 in the crust and 2 ppm and 0.002 in the nodule (Table 1 and S2). Linear scale.

Figure 3. Thallium concentration (a) and percentage of Tl(III) (b) as a function of the ratio of the Mn to Fe concentrations on a weight basis. Black points: FeMn crusts; purple diamonds: nodules.

Figure 4. Raman spectra for δ-MnO_2 and feroxyhite (δ-FeOOH) (a), for δ-MnO_2 and FeMn crusts (b), and for δ-MnO_2 and the 74GTV FeMn crust. The feroxyhite spectrum is from Bellot-Gurlet et al. (2009),[89] δ-MnO_2 is from Manceau et al. (2013),[81], and the FeMn crusts spectrum is the average spectrum of the 10 FeMn crust spectra shown in Figure S6. The peak broadening observed near 700 cm^{-1} in FeMn crusts is attributed to feroxyhite.

Figure 5. Representative Mn K-edge XANES absorption spectra (a) and first derivative (b) of hydrogenetic and diagenetic FeMn deposits. The FeMn crust spectrum is the average of 17 spectra from crusts and two spectra from nodules with an hydrogenetic XRD signature (Fe-vernadite). The 65SL-985cm spectrum is from a buried nodule of the Clarion Clipperton Zone (CCZ) in the central equatorial Pacific with a diagenetic XRD signature (todorokite). (c, d) Combo fits to a database of reference spectra (Table S4 and Ref.[70]).

Figure 6. Tl L_3-edge XANES spectra of $TlNO_3$ and Tl_2O_3 measured at standard resolution with an energy dispersive detector (a) and at standard and high ernergy-resolution (HR-XANES) with a wavelength dispersive detector (five-crystal analyzer) (b, c).

Figure 7. (a,b) Calculated L_3-edge HR-XANES spectra of Tl_2O_3 for dipole-allowed transitions to final states with s symmetry, d symmetry, and s + d symmetry. (c) Calculated L_3-edge HR-XANES spectra of the Tl(1) and Tl(2) sites for Tl_2O_3.

Figure 8. (a) Pure Tl(I) and Tl(III) component spectra obtained by principal component analysis of the 23 HR-XANES spectra of crusts and nodules. (b) Comparison of the two component spectra with the experimental $TlNO_3$ and Tl_2O_3 spectra.

Figure 9. Percentage of Tl(III) as a function of the thallium concentration.

Figure 10. FEFF-calculated HR-XANES spectra of the ^{VI}Tl(III)-TCS and ^{VI}Tl(III)-DES surface complexes (a,b) and the ^{VI}Tl(III)-TCS and ^{IV}Tl(III)-TCS surface complexes.

Figure 11. k^3-weighted Tl L_3-edge EXAFS spectrum of crust MP23-2 (a) and radial structure function (b) with fit.

Figure 12. Geometry-optimized structural position of Tl(I) above a tetrahedral cavity of the MnO_2 layer formed by three edge-sharing Mn octahedra. Mn octahedron = gray; Tl(II) = cyan; oxygen = red, proton = gray.

Table 1. Origin, depositional setting, Mn oxide, percentage of Tl(III) and Tl(I), Tl concentration, and Mn/Fe and Tl/Mn weight ratios of the 29 FeMn samples

Sample name	Source	Setting	Mn oxide[a]	%Tl(III)	%Tl(I)	[Tl] ppm	[Mn]/[Fe] wt	[Tl]/[Mn] at x 10^4
232D-B 0-78	Eastern Indian Ocean	Hydrogenetic crust	Fe-vernadite	79	21	1.5	0.37	0.05
D20-1A	Indian Ocean	Hydrogenetic crust	Fe-vernadite	100	0	190	1.77	1.87
D20-1B	Indian Ocean	Hydrogenetic crust	Fe-vernadite	100	0	151	1.24	1.73
DS4-003A B08-28	Arctic	Hydrogenetic crust	Fe-vernadite	94	6	47	0.26	2.36
D11-A	South Pacific	Hydrogenetic crust	Fe-vernadite	66	34	157	1.22	1.27
37KD-3	CCZ, Pacific Ocean[48]	Hydrogenetic crust	Fe-vernadite	62	38	103	0.92	1.35
122DK	Northeast Atlantic, seamount	Phosphatized crust	Fe-vernadite	79	21	46	0.53	1.17
DS835-1	Northeast Atlantic, seamount	Hydrogenetic crust	Fe-vernadite	74	26	127	0.95	1.60
10DSR young	Central South Pacific	Hydrogenetic crust	Fe-vernadite	88	12	252	1.92	2.32
10DSR old	Central South Pacific	Phosphatized crust	Fe-vernadite	91	9	319	3.32	2.92
39DK	Central North Pacific	Hydrogenetic crust	Fe-vernadite	77	23	278	2.55	2.30
40DS	Central North Pacific	Hydrogenetic crust	Fe-vernadite	91	9	135	1.26	1.57
74GTV	Central Indian ridge	Hydrogenetic/hydrothermal crust	Fe-vernadite	79	21	39	0.71	0.59
MP-1	Manihiki Plateau, South West Pacific	Hydrogenetic crust	Fe-vernadite	85	15	97	0.92	1.27
MP-14	Manihiki Plateau, South West Pacific	Hydrogenetic crust	Fe-vernadite	88	12	157	1.04	2.02
MP-27-3	Manihiki Plateau, South West Pacific	Phosphatized crust	Fe-vernadite	75	25	97	1.03	1.62
MP-23-2	Manihiki Plateau, South West Pacific	Phosphatized crust	Fe-vernadite (M); todorokite (m)	95	5	283	3.95	2.64
BS-surface[b]	Baltic Sea	Nodule	Not measured	0	100	2	1.06	0.03
BS-bulk	Baltic Sea	Nodule	10 Å and 7 Å vernadite (M); todorokite (m)	19	82	4	2.61	0.04
KG1313	Peru Basin	Nodule, sediment surface	Fe-vernadite (m); 10 Å and 7 Å vernadite (M); todorokite (M)	96	4	22	30.33	0.13
EBS8-6	CCZ, Verma zone	Hydrogenetic nodule	Fe-vernadite (M); 10 Å vernadite (M); 7 Å vernadite (m)	77	23	10	0.41	0.27
44KG-2	CCZ, Pacific Ocean[48,51]	Nodule, sediment surface[c]	Fe-vernadite (M); 10 Å vernadite (M); 7 Å vernadite (m); todorokite (m)	74	26	112	6.26	0.91

21KG-1(n)	CCZ, Pacific Ocean[51]	Nodule, sediment surface[c]	Fe-vernadite (M); 10 Å and 7 Å vernadite (M); todorokite (m)	100	0	44	7.38	0.34
107KG-1-16cm	CCZ, Pacific Ocean[51]	Nodule, 16 cm sediment depth	Todorokite	79	21	11	2.46	0.13
107KG-36cm	CCZ, Pacific Ocean[51]	Nodule, 36 cm sediment depth	Todorokite	77	23	5	1.42	0.09
09KL-44-49cm	CCZ, Pacific Ocean[51]	Nodule, 44-49 cm sediment depth	10 Å vernadite (M); todorokite (M); 7 Å vernadite (m)	78	22	15	8.12	0.12
22KL-1-530cm	CCZ, Pacific Ocean[51]	Nodule, 530 cm sediment depth	Todorokite	39	61	2	8.95	0.02
22KL-2-801cm	CCZ, Pacific Ocean[51]	Nodule, 801 cm sediment depth	Todorokite	49	50	2	8.61	0.02
65SL-985cm	CCZ, Pacific Ocean[51]	Nodule, 985 cm sediment depth	Todorokite	31	69	2	6.19	0.02

[a]XRD Abundance. [b]A portion of the 1mm surface layer was sampled with a drill. M=major, m=minor. [c]Hydrogenetic growth structures are observed by EPMA.

Table 2. Fractional and average valence states of Mn obtained from the Combo fit of XANES derivatives in the 6535–6570 eV interval.

	Mn(IV)	Mn(III)	Mn(II)	Average[a]	*NSS*[b]
Hollandite					
Manceau et al. (2012)	0.82	0.16	0.02	3.81 ± 0.04	
This study	0.873	0.110	0.018	3.85 ± 0.06	9.5×10^{-3}
Psilomelane					
Manceau et al. (2012)	0.81	0.16	0.04	3.77 ± 0.04	
This study	0.858	0.106	0.036	3.82 ± 0.07	9.4×10^{-3}
Todorokite-Japan					
Manceau et al. (2012)	0.78	0.21	0.01	3.78 ± 0.04	
This study	0.881	0.076	0.043	3.84 ± 0.10	14.7×10^{-3}
(Fe)-vernadite_average	0.975	-	0.025	3.95 ± 0.05	6.3×10^{-3}
BS-bulk	0.855	0.079	0.066	3.79 ± 0.08	9.3×10^{-3}
KG1313	0.810	0.144	0.046	3.76 ± 0.07	9.6×10^{-3}
44KG-2	0.918	0.045	0.037	3.88 ± 0.08	7.7×10^{-3}
21KG-1(n)	0.868	0.095	0.036	3.83 ± 0.08	9.9×10^{-3}
107KG-1-16cm	0.897	0.078	0.025	3.87 ± 0.07	7.1×10^{-3}
107KG-36cm	0.870	0.113	0.018	3.85 ± 0.08	8.6×10^{-3}
22KL-1-530cm	0.801	0.166	0.033	3.77 ± 0.08	9.9×10^{-3}
22KL-2-801cm	0.790	0.177	0.033	3.76 ± 0.07	9.1×10^{-3}
65SL-985cm	0.759	0.219	0.022	3.74 ± 0.07	7.5×10^{-3}

[a]The precision on the variation of the AOS between two samples is about one half as good as the reported accuracy of estimation (Figure S3 and Table S4). [b]The *NSS* values of the Combo fits for the normalized XANES spectra are in the 10^{-5} range.

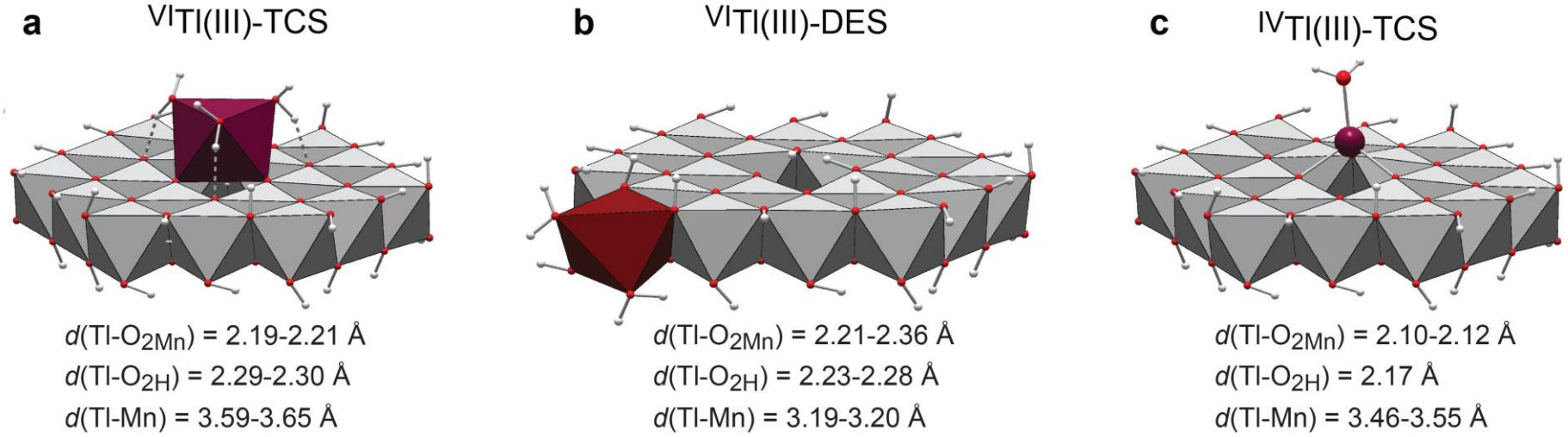
a
VITI(III)-TCS
d(Tl-O2Mn) = 2.19-2.21 Å
d(Tl-O2H) = 2.29-2.30 Å
d(Tl-Mn) = 3.59-3.65 Å
b
VITI(III)-DES
d(Tl-O2Mn) = 2.21-2.36 Å
d(Tl-O2H) = 2.23-2.28 Å
d(Tl-Mn) = 3.19-3.20 Å
c
IVTI(III)-TCS
d(Tl-O2Mn) = 2.10-2.12 Å
d(Tl-O2H) = 2.17 Å
d(Tl-Mn) = 3.46-3.55 Å

Figure 1

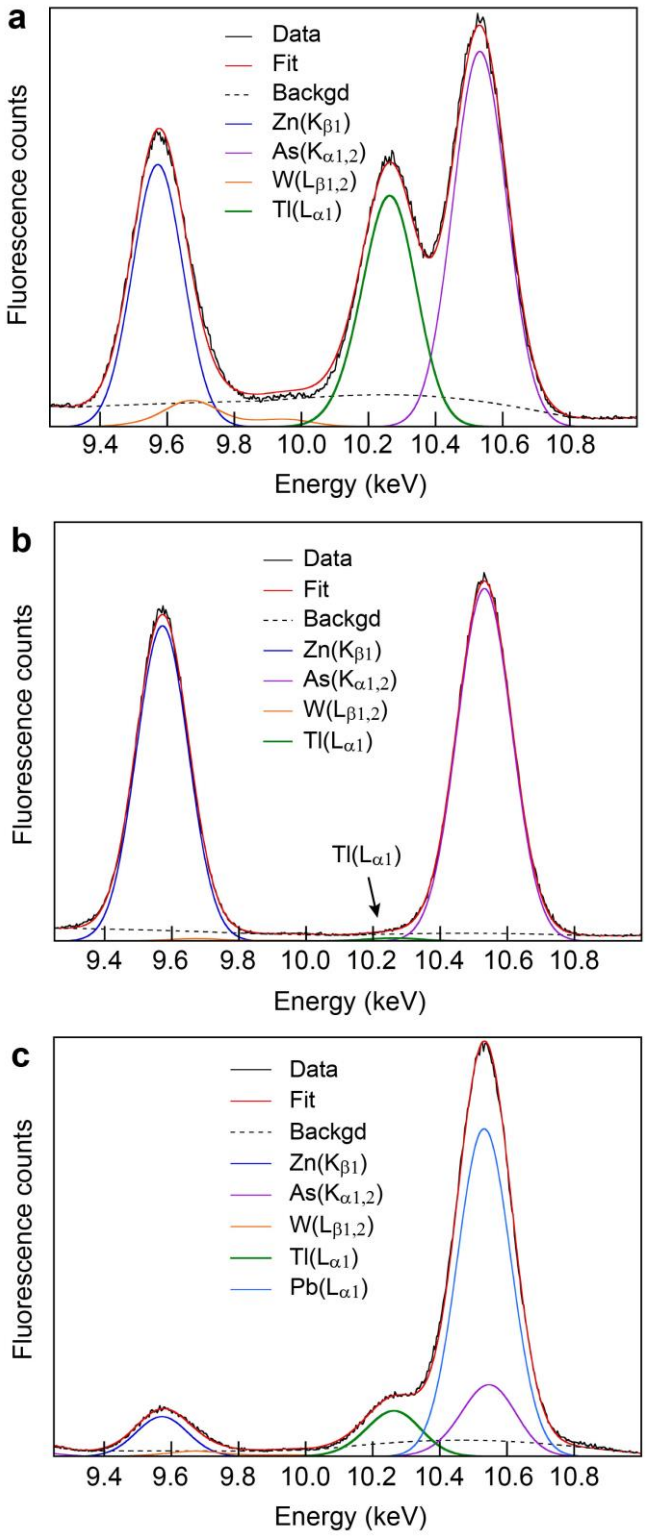
a
Data
Fit
Backgd
Zn(Kβ1)
As(Kα1,2)
W(Lβ1,2)
Tl(Lα1)
Fluorescence counts
9.4 9.6 9.8 10.0 10.2 10.4 10.6 10.8
Energy (keV)
b
Data
Fit
Backgd
Zn(Kβ1)
As(Kα1,2)
W(Lβ1,2)
Tl(Lα1)
Tl(Lα1)
Fluorescence counts
9.4 9.6 9.8 10.0 10.2 10.4 10.6 10.8
Energy (keV)
c
Data
Fit
Backgd
Zn(Kβ1)
As(Kα1,2)
W(Lβ1,2)
Tl(Lα1)
Pb(Lα1)
Fluorescence counts
9.4 9.6 9.8 10.0 10.2 10.4 10.6 10.8
Energy (keV)

Figure 2

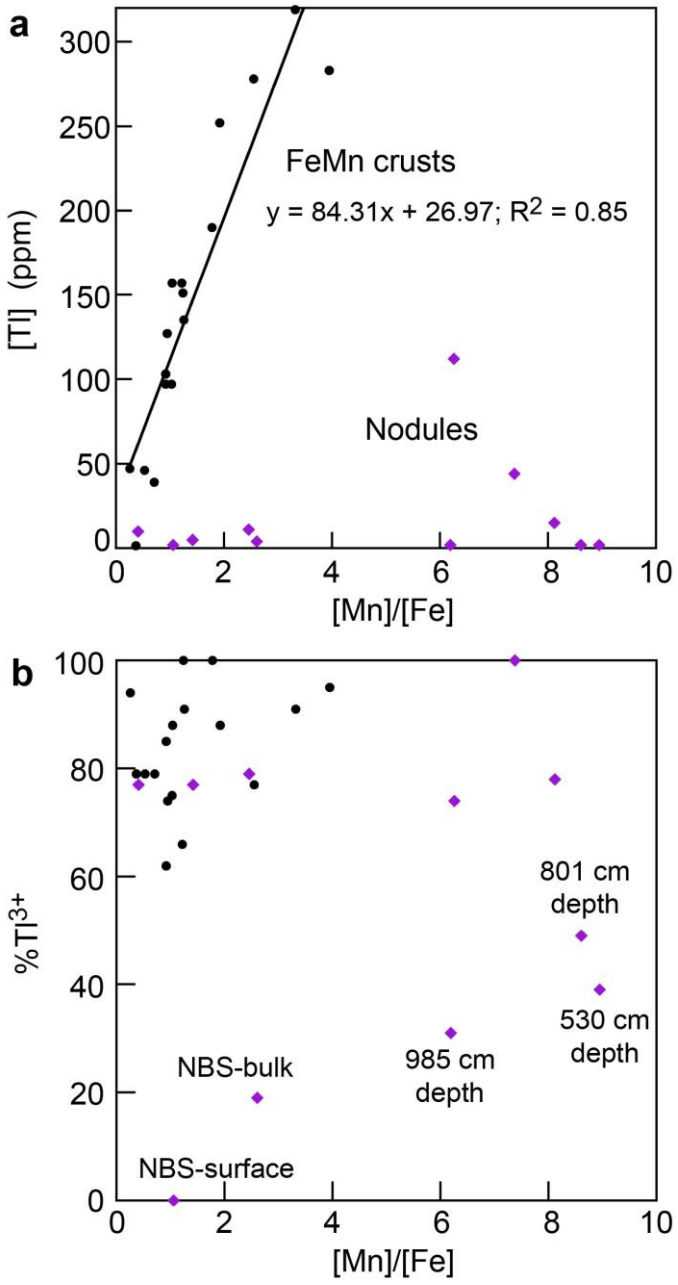
a
300
250
200
150
100
50
0
[Tl] (ppm)
FeMn crusts
y = 84.31x + 26.97; R2 = 0.85
Nodules
0
2
4
6
8
10
[Mn]/[Fe]
b
100
80
60
40
20
0
%Tl3+
801 cm
depth
530 cm
depth
985 cm
depth
NBS-bulk
NBS-surface
0
2
4
6
8
10
[Mn]/[Fe]

Figure 3

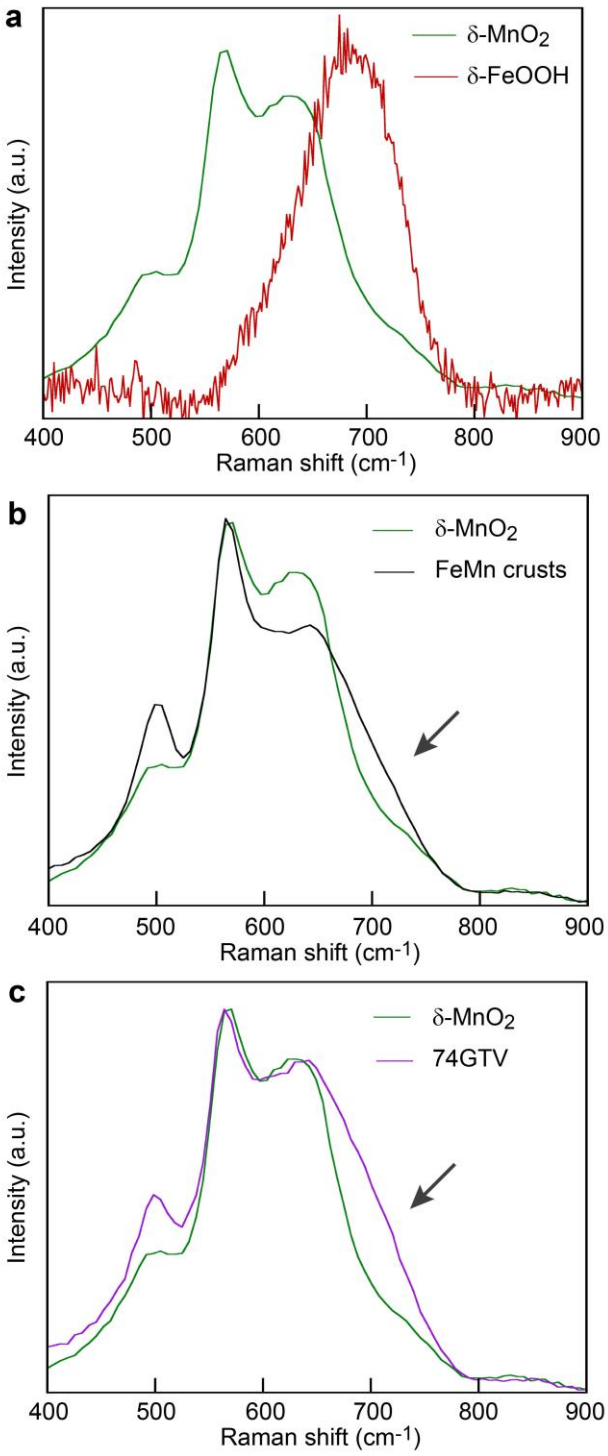
a
δ-MnO2
δ-FeOOH
Intensity (a.u.)
400
500
600
700
800
900
Raman shift (cm-1)
b
δ-MnO2
FeMn crusts
Intensity (a.u.)
400
500
600
700
800
900
Raman shift (cm-1)
c
δ-MnO2
74GTV
Intensity (a.u.)
400
500
600
700
800
900
Raman shift (cm-1)

Figure 4

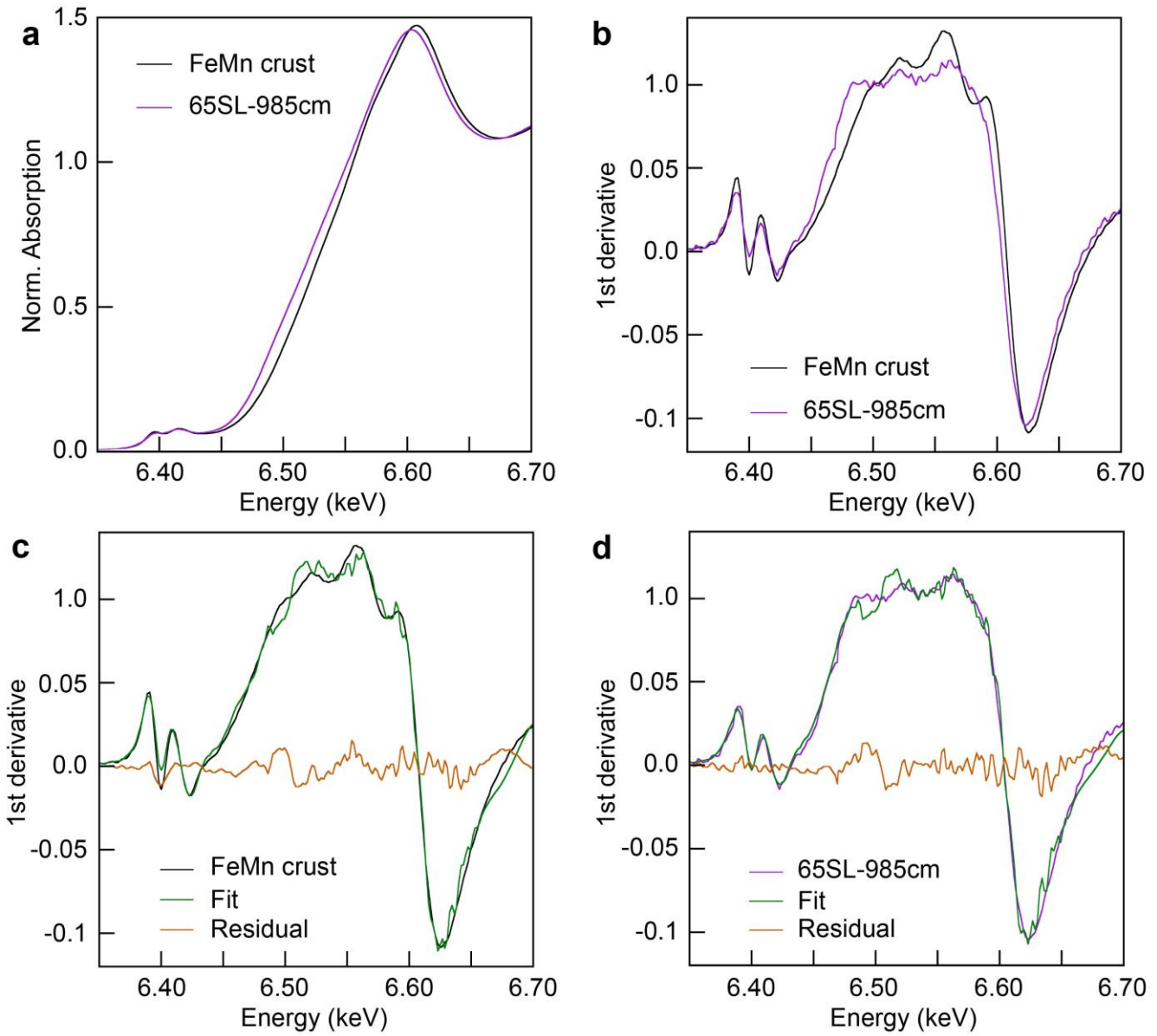
a
FeMn crust
65SL-985cm
Norm. Absorption
Energy (keV)
b
1st derivative
FeMn crust
65SL-985cm
Energy (keV)
c
1st derivative
FeMn crust
Fit
Residual
Energy (keV)
d
1st derivative
65SL-985cm
Fit
Residual
Energy (keV)

Figure 5

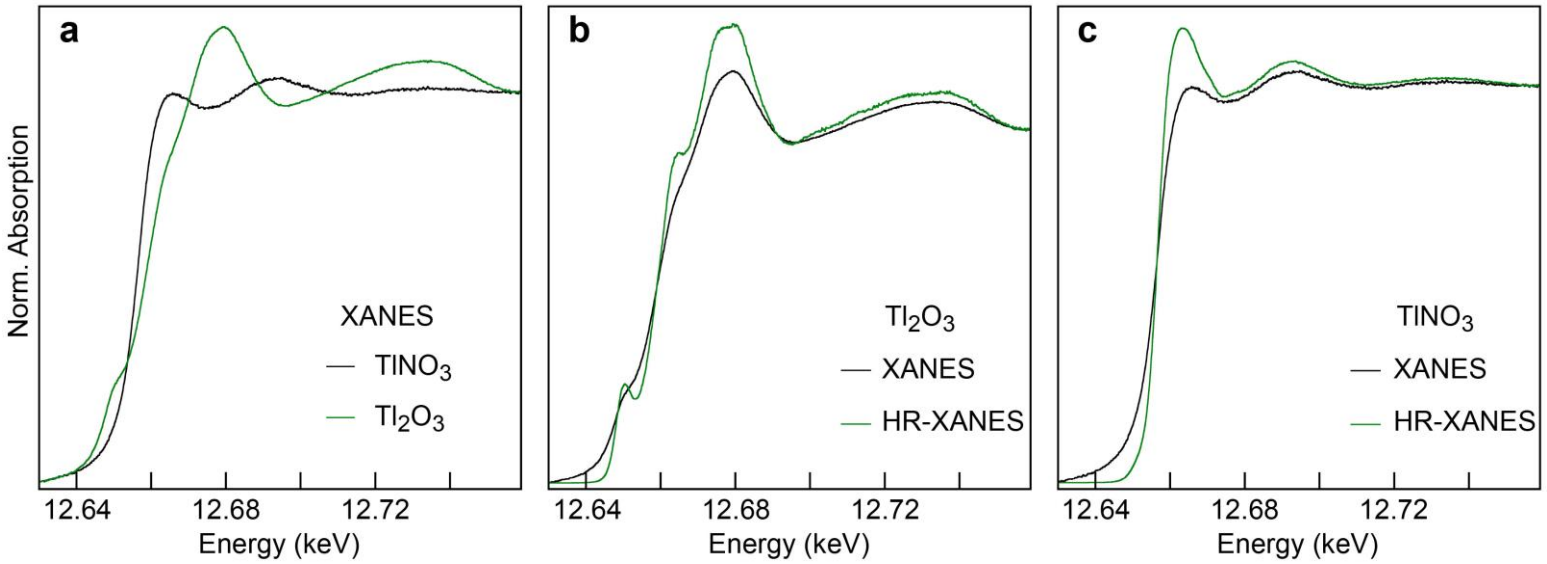

Figure 6

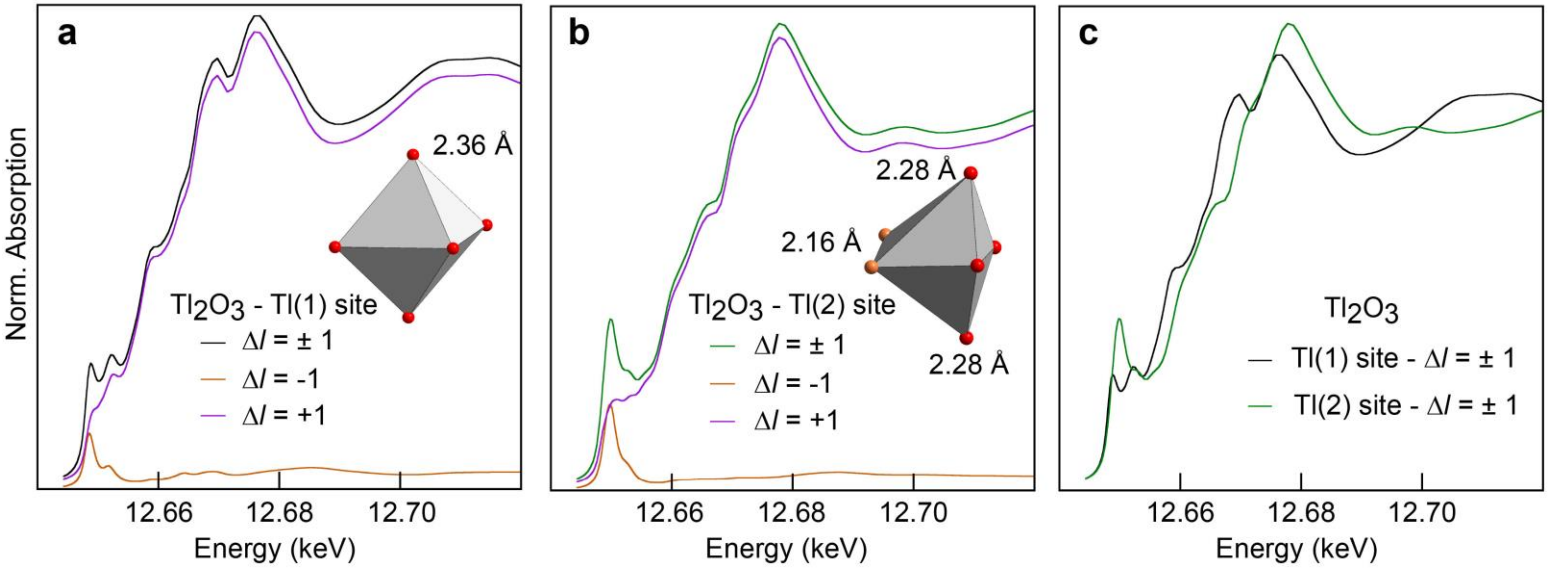

Figure 7

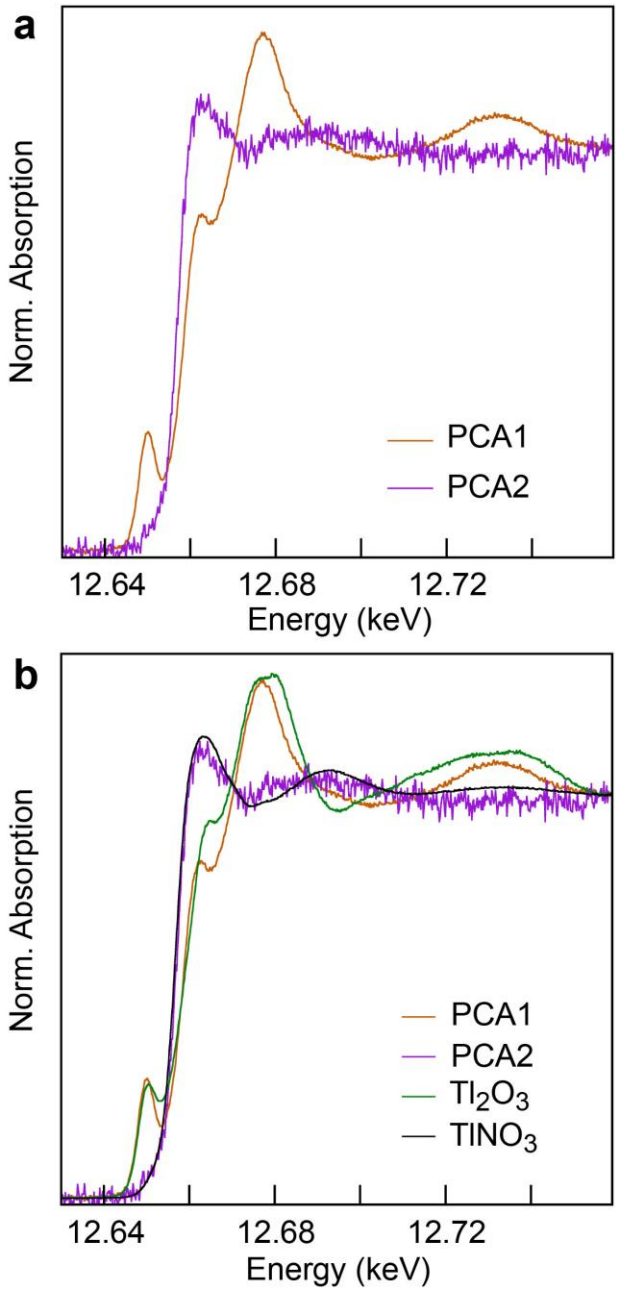
a
Norm. Absorption
PCA1
PCA2
12.64
12.68
12.72
Energy (keV)
b
Norm. Absorption
PCA1
PCA2
Tl2O3
TlNO3
12.64
12.68
12.72
Energy (keV)

Figure 8

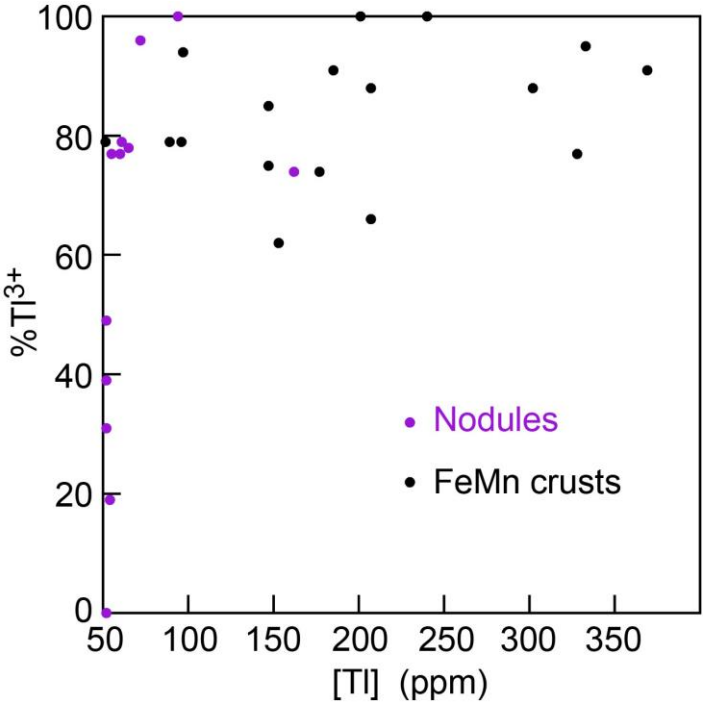
100
80
60
40
20
0
%Tl3+
50
100
150
200
250
300
350
[Tl] (ppm)
Nodules
FeMn crusts

Figure 9

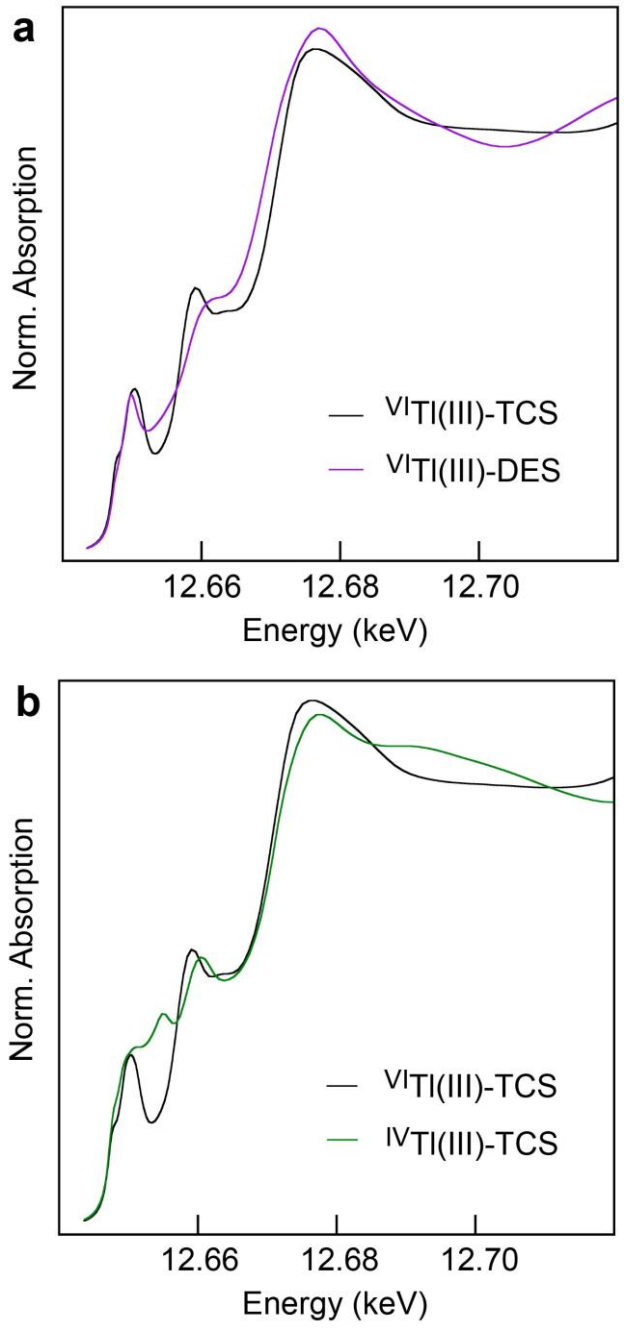
a
Norm. Absorption
VITl(III)-TCS
VITl(III)-DES
12.66
12.68
12.70
Energy (keV)
b
Norm. Absorption
VITl(III)-TCS
IVTl(III)-TCS
12.66
12.68
12.70
Energy (keV)

Figure 10

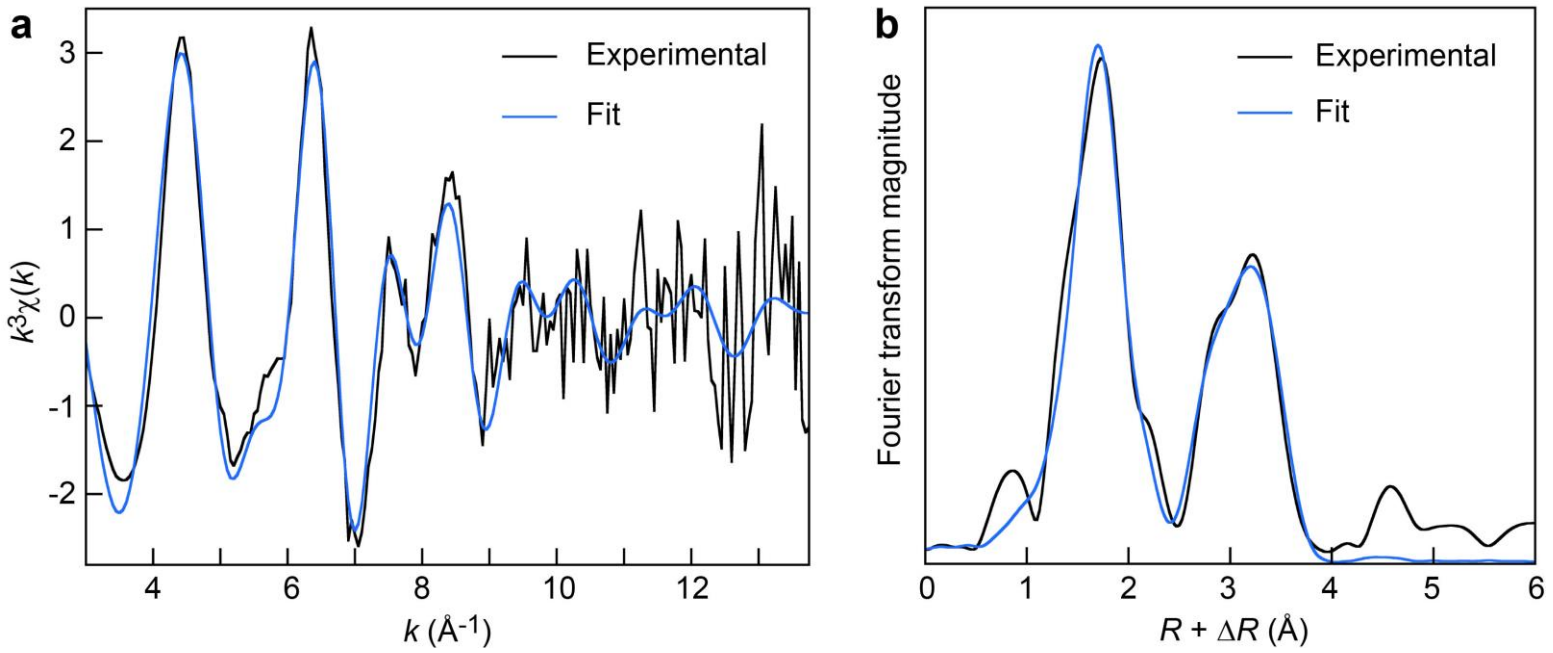
a
Experimental
Fit
$k^3\chi(k)$
k (Å^{-1})
b
Experimental
Fit
Fourier transform magnitude
$R + \Delta R$ (Å)

Figure 11

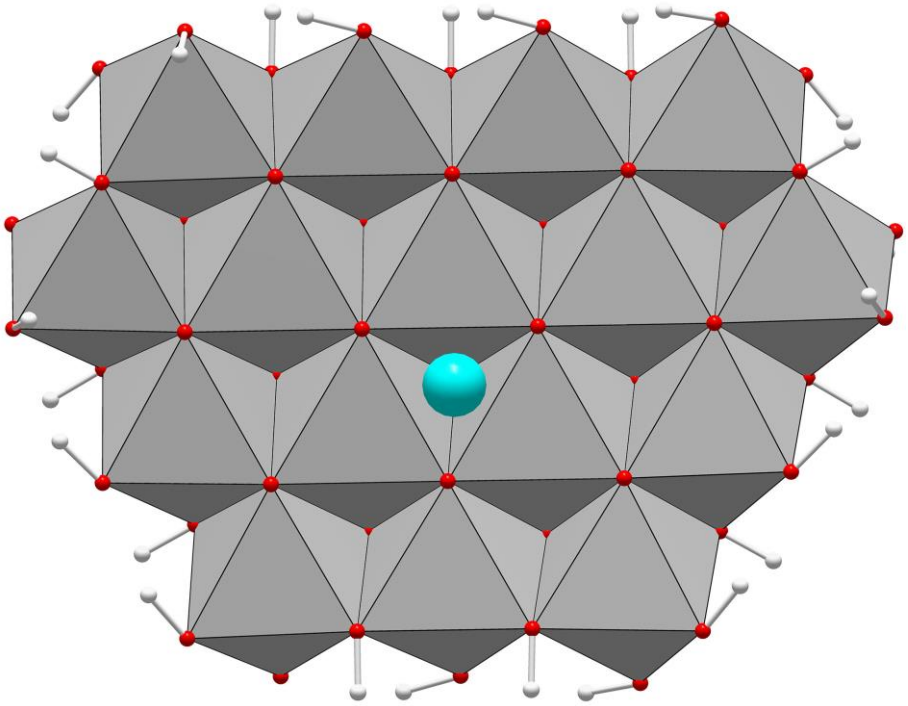

Figure 12

Supplementary Information

Crystal Chemistry of Thallium in Marine Ferromanganese Deposits

Alain Manceau*[1], Alexandre Simionovici[1], Nathaniel Findling[1], Pieter Glatzel[2], Blanka Detlefs[2], Anna V. Wegorzewski[3], Thomas Kuhn[3], Kira Mizell[4], James R. Hein[4], and Andrea Koschinsky*[5]

[1]Université Grenoble Alpes, ISTerre, CNRS, F-38058 Grenoble, France
[2]European Synchrotron Radiation Facility (ESRF), F-38000 Grenoble, France
[3]Federal Institute for Geoscience and Natural Resources (BGR), Stilleweg 2, D-30655 Hannover, Germany
[4]U.S. Geological Survey, Pacific Coastal and Marine Science Center, Santa Cruz, California 95060, United States
[5]Department of Physics and Earth Sciences, Jacobs University Bremen, Bremen 28759, Germany

Corresponding Authors : alain.manceau@univ-grenoble-alpes.fr; a.koschinsky@jacobs-university.de

DFT modeling of the surface complexes

The equilibrium geometries of the Tl(III)-DES and Tl(III)-TCS complexes on the Mn18 nanosheets were calculated using ORCA[1] and with the same high-level quantum chemical methods as described in detail previously for the sorption of 3d transition metals and Pb(II) on δ-MnO_2.[2] Briefly, the electronic exchange-correlation energy was calculated with the Perdew Burke and Ernzerhof functional PBE0 (also called PBE1PBE)[3,4] and atom-pairwise dispersion interactions were described with the D3BJ method[5] applied to all atoms. The valence electronic configurations of all atoms were treated with the all-electron polarized def2-TZVP basis sets of triple ζ quality,[6] in combination with the Coulomb fitting auxiliary def2 /J basis sets.[7] The scalar relativity of Tl was accounted for by replacing the 60 innermost electrons with the def2-ECP effective core potential (ECP), as obtained from the Stuttgart pseudopotential library. The atom-pairwise dispersion correction D3BJ[5] was applied to all atoms. The solvation model based on density (SMD)[8] with water as the solvent was applied to all calculations.

Supplementary References

(1) Neese, F. Software Update: The ORCA Program System-Version 5.0. *Wiley Interdiscip. Rev. Comput. Mol. Sci.* **2022**, e1606.
(2) Manceau, A.; Steinmann, S. N. Nature of High- and Low-Affinity Metal Surface Sites on Birnessite Nanosheets. *ACS Earth Space Chem.* **2021**, *5*, 66–76.
(3) Adamo, C.; Barone, V. Toward Reliable Density Functional Methods without Adjustable Parameters: The PBE0 Model. *J. Chem. Phys.* **1999**, *110*, 6158–6170.
(4) Perdew, J. P.; Burke, K.; Ernzerhof, M. Generalized Gradient Approximation Made Simple. *Phys. Rev. Lett.* **1996**, *77*, 3865–3868.
(5) Grimme, S.; Ehrlich, S.; Goerigk, L. Effect of the Damping Function in Dispersion Corrected Density Functional Theory. *J. Comput. Chem.* **2011**, *32*, 1456–1465.

(6) Weigend, F.; Ahlrichs, R. Balanced Basis Sets of Split Valence, Triple Zeta Valence and Quadruple Zeta Valence Quality for H to Rn: Design and Assessment of Accuracy. *Phys. Chem. Chem. Phys.* **2005**, *7*, 3297–3305.
(7) Weigend, F. Accurate Coulomb-Fitting Basis Sets for H to Rn. *Phys. Chem. Chem. Phys.* **2006**, *8*, 1057–1065.
(8) Marenich, A. V.; Cramer, C. J.; Truhlar, D. G. Universal Solvation Model Based on Solute Electron Density and on a Continuum Model of the Solvent Defined by the Bulk Dielectric Constant and Atomic Surface Tensions. *J. Phys. Chem. B* **2009**, *113*, 6378–6396.
(9) Hlawatsch, S.; Kersten, M.; Garbe-Schönberg, C. D.; Lechtenberg, F.; Manceau, A.; Tamura, N.; Kulik, D. A.; Harff, J.; Suess, E. Trace Metal Fluxes to Ferromanganese Nodules from the Western Baltic Sea as a Record for Long-Term Environmental Changes. *Chem. Geol.* **2002**, *182*, 697–710.
(10) Hlawatsch, S.; Neumann, T.; van den Berg, C. M. G.; Kersten, M.; Harff, J.; Suess, E. Fast-Growing, Shallow-Water Ferro-Manganese Nodules from the Western Baltic Sea: Origin and Modes of Trace Element Incorporation. *Mar. Geol.* **2002**, *182*, 373–387.
(11) Rovezzi, M.; Lapras, C.; Manceau, A.; Glatzel, P.; Verbeni, R. High Energy-Resolution x-Ray Spectroscopy at Ultra-High Dilution with Spherically Bent Crystal Analyzers of 0.5 m Radius. *Rev. Sci. Instr.* **2017**, *88*, 013108.
(12) Manceau, A.; Marcus, M.; Lenoir, T. Estimating the Number of Pure Chemical Components in a Mixture by X-Ray Absorption Spectroscopy. *J. Synchrotron Radiat.* **2014**, *21*, 1140–1147.
(13) Wegorzewski, A. V.; Grangeon, S.; Webb, S. M.; Heller, C.; Kuhn, T. Mineralogical Transformations in Polymetallic Nodules and the Change of Ni, Cu and Co Crystal-Chemistry upon Burial in Sediments. *Geochim. Cosmochim. Acta* **2020**, *282*, 19–37.
(14) Li, J. W.; Li, L.; Bai, S. J.; Chen, S.; Xu, H. C.; Ta, K. W.; Qu, Y. G.; Wang, Y. G.; Yao, H. Q.; Dong, Y. H.; Dasgupta, S.; Du, M. R.; Liu, S. Q.; Lin, F. Y.; Peng, X. T. Geochemical and Molecular Characteristics of Ferromanganese Deposits and Surrounding Sediments in the Mariana Trench: An Implication for the Geochemical Mn Cycle in Sedimentary Environments of the Trench Zone. *Geochim. Cosmochim. Acta* **2021**, *310*, 155–168.
(15) Manceau, A.; Marcus, M. A.; Grangeon, S. Determination of Mn Valence States in Mixed-Valent Manganates by XANES Spectroscopy. *Am. Miner.* **2012**, *97*, 816–827.
(16) Glans, P. A.; Learmonth, T.; Smith, K. E.; Guo, J.; Walsh, A.; Watson, G. W.; Terzi, F.; Egdell, R. G. Experimental and Theoretical Study of the Electronic Structure of HgO and Tl_2O_3. *Phys. Rev. B* **2005**, *71*, 235109.

Supplementary Figures

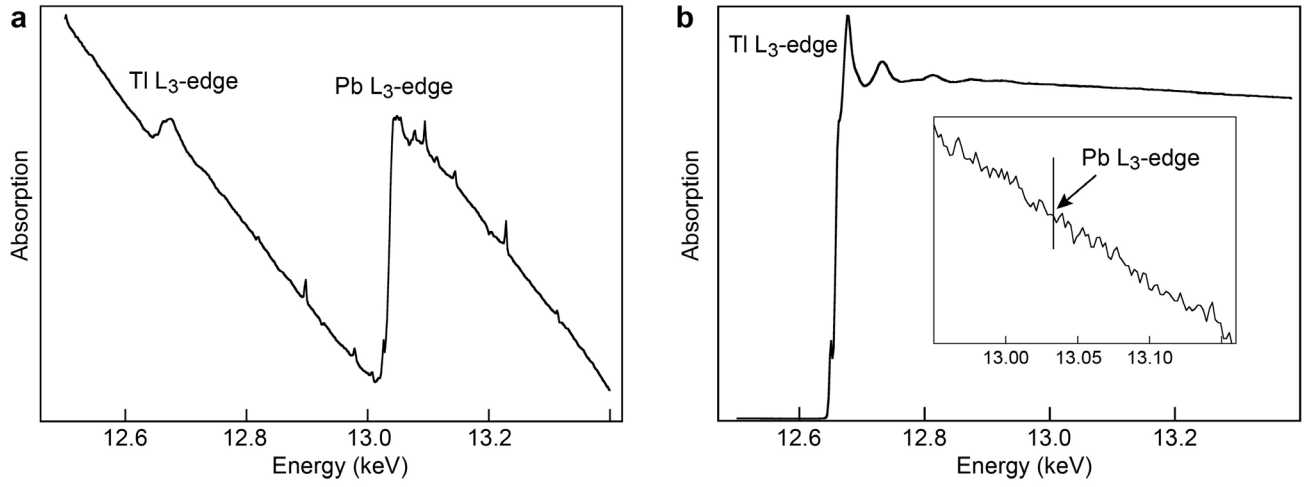

Figure S1. X-ray absorption spectrum of crust MP23-2 measured with a photodiode (a) and with a five-crystal analyzer (b). [Tl] = 283 ppm, [Pb] = 1413 ppm.

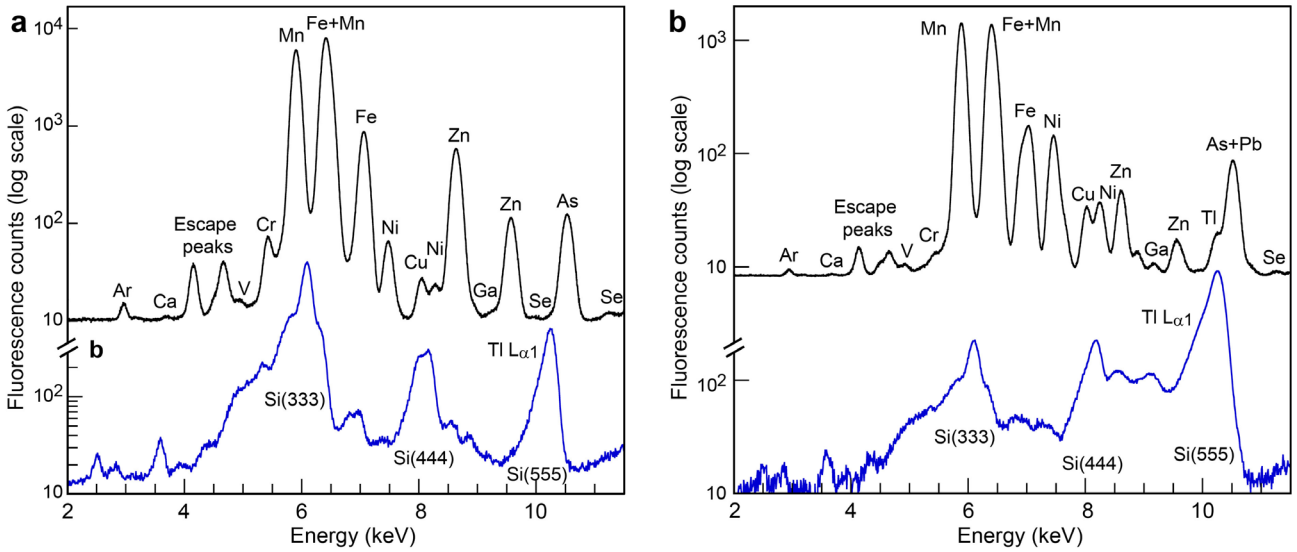

Figure S2. X-ray fluorescence spectra of the surface layer of Baltic Sea nodule[9,10] (a) and crust MP23-2 (b) measured with an energy dispersive detector only (black lines) and with a five-crystal Si(111) analyzer[11] tuned to the energy of the Tl $L_{\alpha 1}$ fluorescence line and placed between sample and an energy dispersive detector (blue line). The Baltic Sea nodule has [Tl] = 2 ppm, [Mn] = 15.6 wt %, and [Fe]= 14.7 wt % (BS-surface, Table S2). Crust MP23-2 has [Tl] = 283 ppm, [Mn] = 28.9 wt %, and [Fe]= 7.3 wt %. The peak at about 10,270 eV corresponds to the Tl $L_{\alpha 1}$ line diffracted by the Si(555) reflection of the analyzer, and the peaks at 8,100 eV and 6,100 eV correspond to the fluorescence lines from the matrix diffracted by the Si(444) and Si(333) reflections.

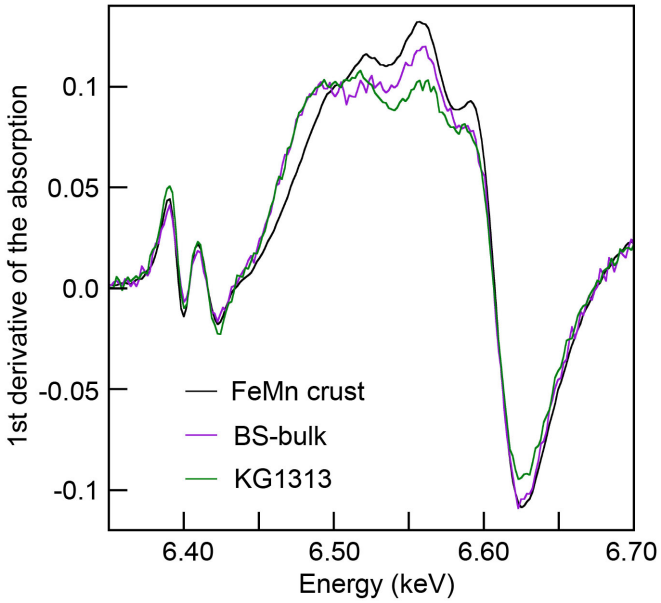

Figure S3. First derivative of the Mn-XANES spectra of FeMn crust (AOS = 3.95 ± 0.05), BS_bulk (AOS = 3.79 ± 0.08), and KG1313 (3.76 ± 0.07). The accuracy of the Mn AOS given after the mean value in parenthesis was estimated to be equal to the variation of the best-fit AOS value when the fit

residual (*NSS*) was increased by 20%. We show with this example that this criterion is most conservative and that the precision on the variation of the AOS is actually better, on the order of 0.03 to 0.04 v.u.

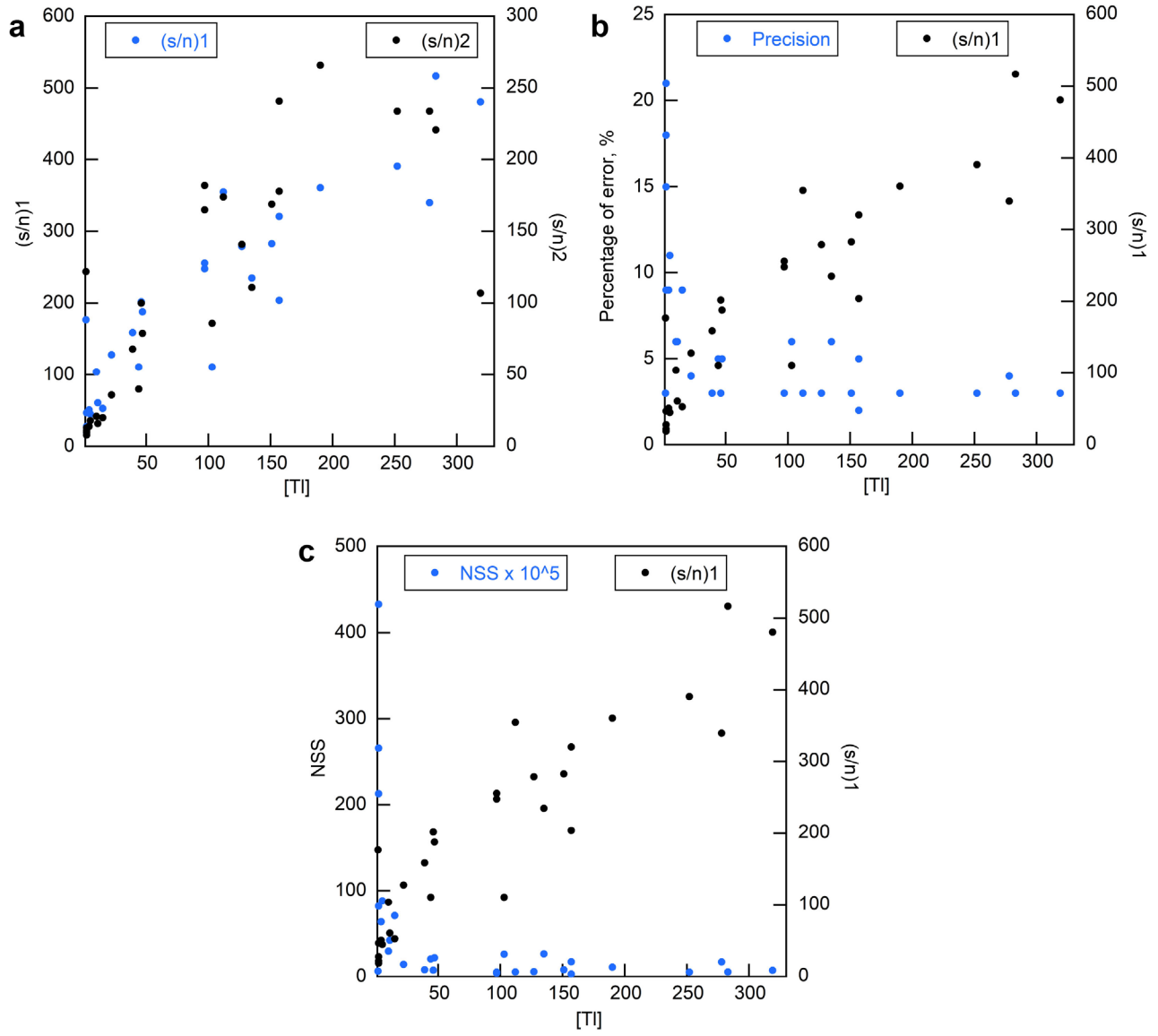

Figure S4. (a) Positive relationship between the signal-to-noise (s/n) ratio of the HR-XANES spectra and the Tl concentration. (b) Percentage of error on the determination of the proportions of Tl(I) and Tl(III) by HR-XANES as a function of the Tl concentration. The error bar follows a power-law with [Tl], decreasing when [Tl] increases, whereas (s/n) increases proportionally with [Tl]. (c) Variation of the fit residual (*NSS*) with [Tl]. *NSS* also follows a negative power-law with [Tl]. The lower *NSS*, the lower is the error on %Tl(I) and %Tl(III). *NSS* is the normalized sum-squared difference between the data and fit expressed as $\Sigma[(y_{data}-y_{fit})^2]/\Sigma(y_{data}^2)$, and $(s/n)_1$ and $(s/n)_2$ are the signal-to-noise ratios of the data measured with the two following expressions[12]:

$$(s/n)_1 = \sqrt{\frac{\langle S^2 \rangle}{\mathrm{Var}(S-F)}}$$

$$(s/n)_2 = \sqrt{\frac{\langle S \rangle}{\mathrm{Var}((S-F)/\sqrt{S})}}$$

where S and F are the original signal and filtered (i.e., de-noised) data, respectively, $\langle \cdots \rangle$ is a mean over the energy range, and Var(x) is the variance of x sampled over the energy range. The de-noising algorithm is detailed in Ref.[12]

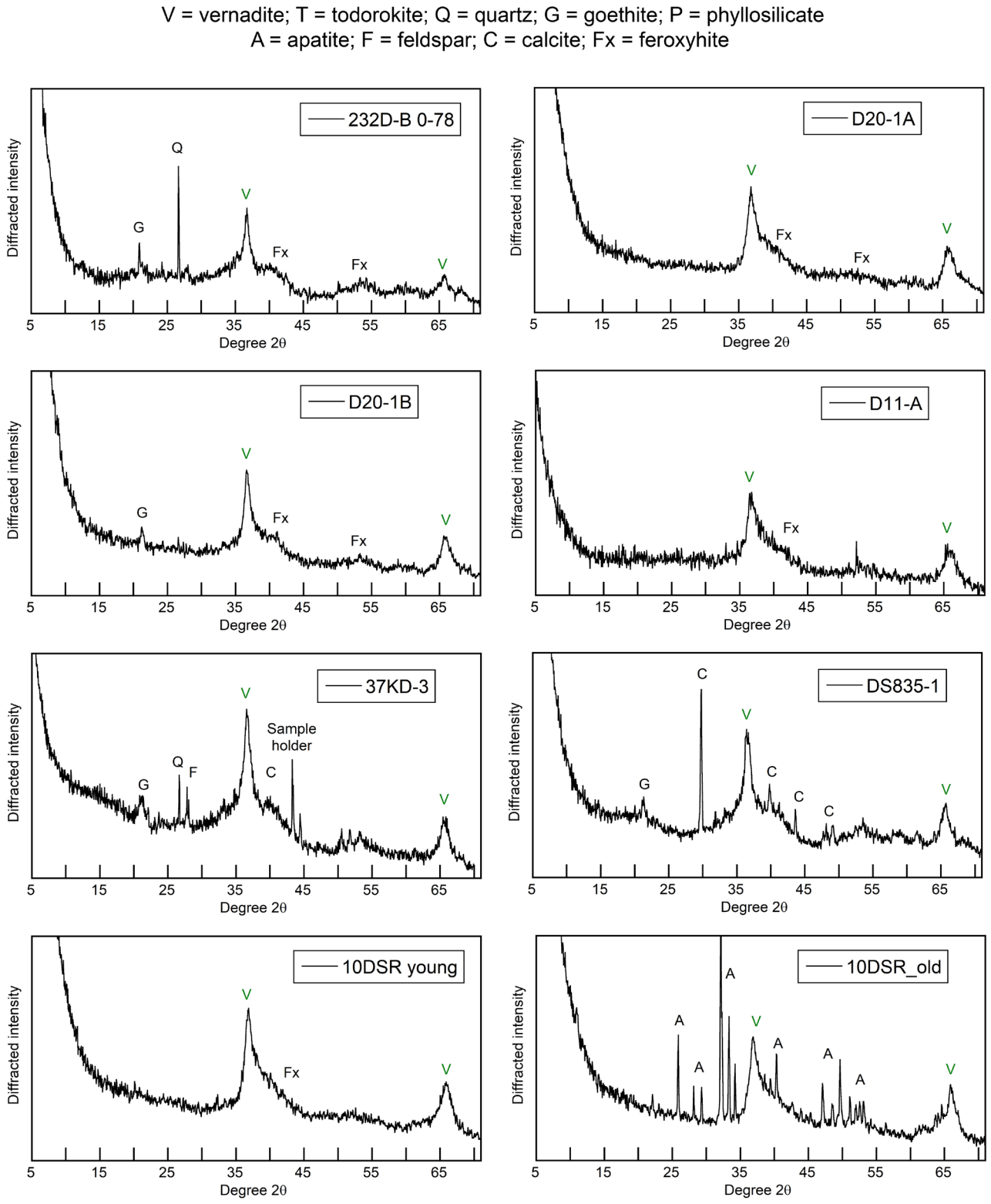

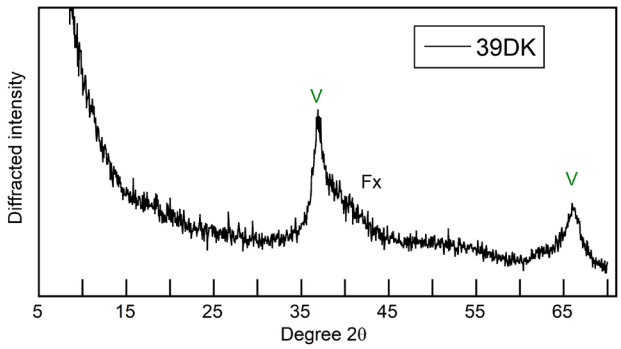
39DK
Diffracted intensity
V
Fx
V
5 15 25 35 45 55 65
Degree 2θ

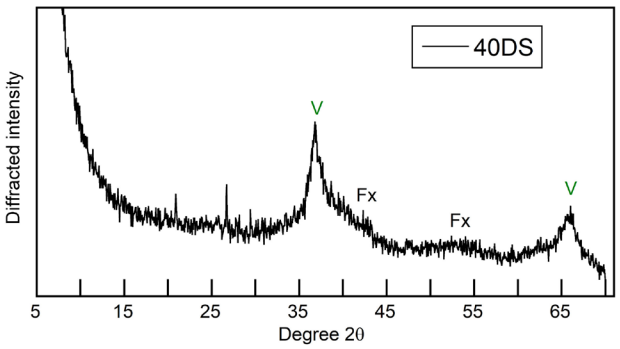
40DS
Diffracted intensity
V
Fx
Fx
V
5 15 25 35 45 55 65
Degree 2θ

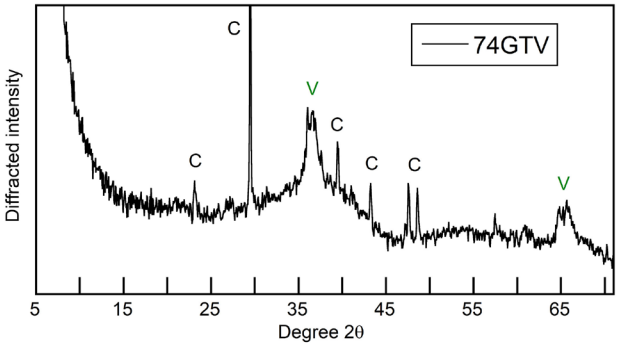
74GTV
Diffracted intensity
C
V
C
C
C
C
V
5 15 25 35 45 55 65
Degree 2θ

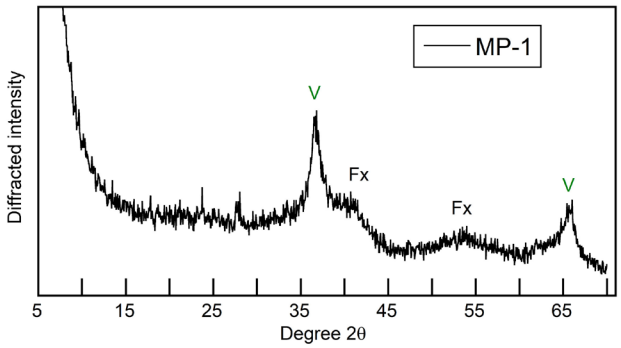
MP-1
Diffracted intensity
V
Fx
Fx
V
5 15 25 35 45 55 65
Degree 2θ

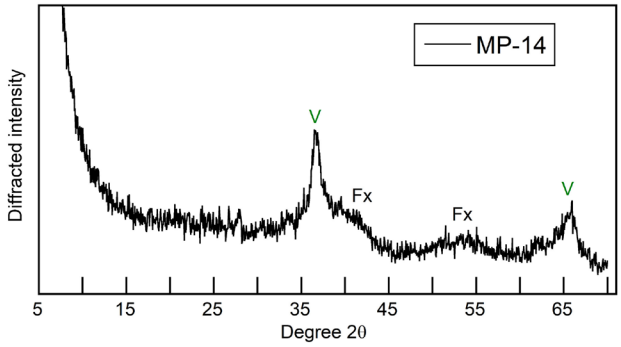
MP-14
Diffracted intensity
V
Fx
Fx
V
5 15 25 35 45 55 65
Degree 2θ

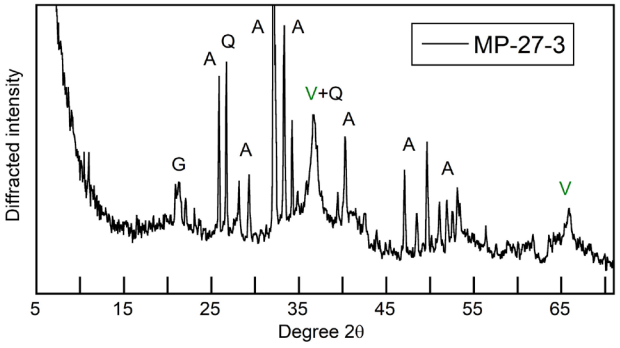
MP-27-3
Diffracted intensity
G
A
Q
A
A
A
V+Q
A
A
A
V
5 15 25 35 45 55 65
Degree 2θ

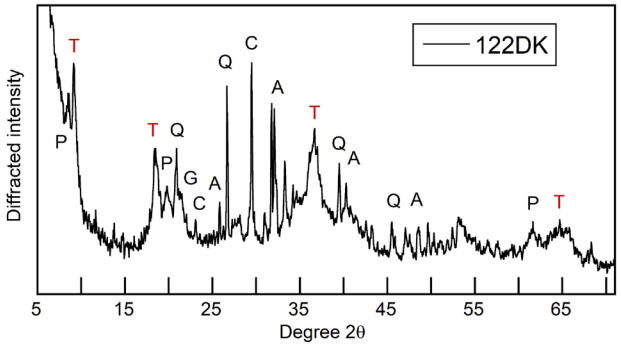
122DK
Diffracted intensity
P
T
T
P
Q
G
C
A
Q
C
A
T
Q
A
Q
A
P
T
5 15 25 35 45 55 65
Degree 2θ

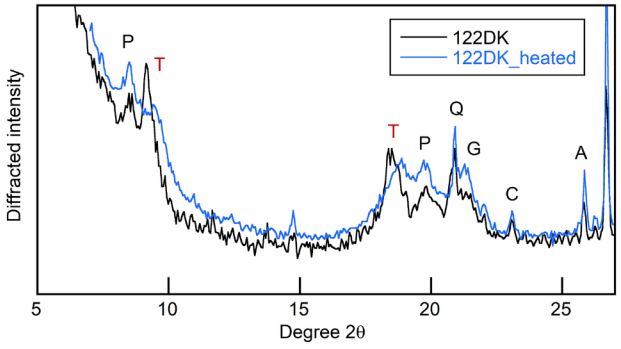
122DK
122DK_heated
Diffracted intensity
P
T
T
P
Q
G
C
A
5 10 15 20 25
Degree 2θ

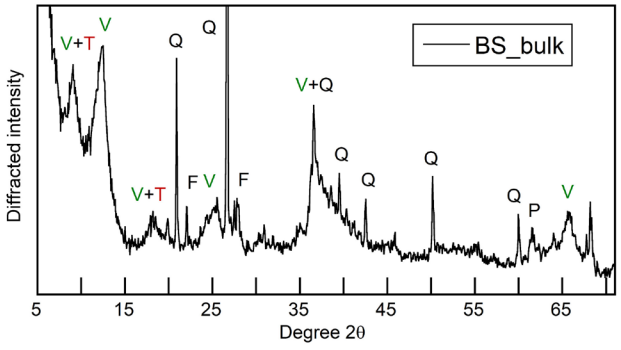
BS_bulk
Diffracted intensity
V+T
V
Q
Q
V+Q
V+T
F
V
F
Q
Q
Q
Q
P
V
5 15 25 35 45 55 65
Degree 2θ

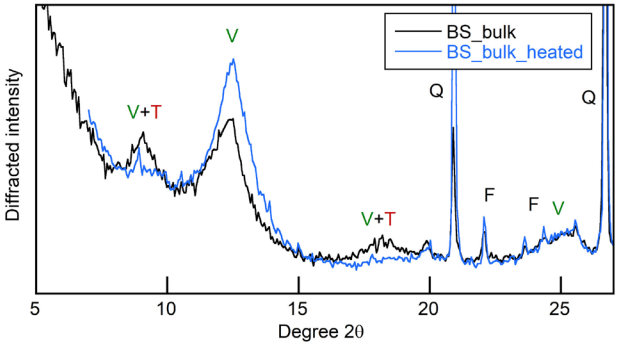
BS_bulk
BS_bulk_heated
Diffracted intensity
V
V+T
Q
Q
V+T
F
F
V
5 10 15 20 25
Degree 2θ

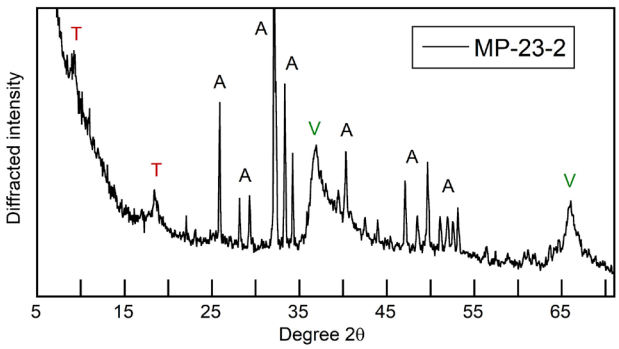
MP-23-2
Diffracted intensity
Degree 2θ
T
A
V

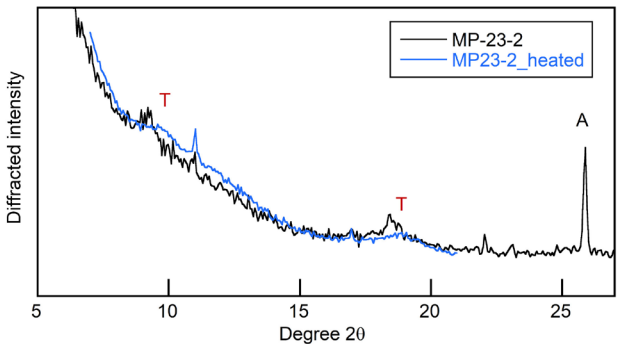
MP-23-2
MP23-2_heated
Diffracted intensity
Degree 2θ
T
A

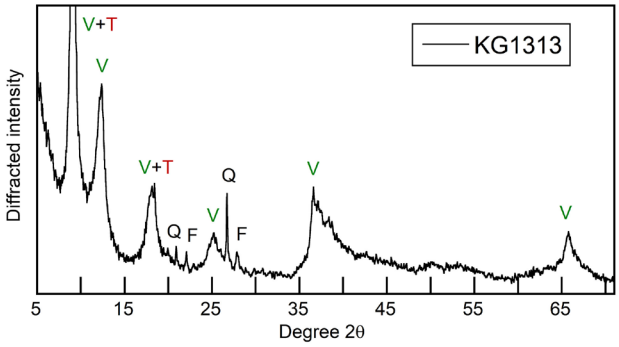
KG1313
Diffracted intensity
Degree 2θ
V+T
V
Q
F

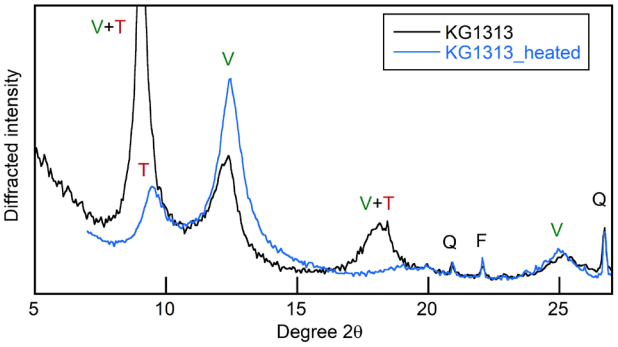
KG1313
KG1313_heated
Diffracted intensity
Degree 2θ
V+T
V
T
Q
F

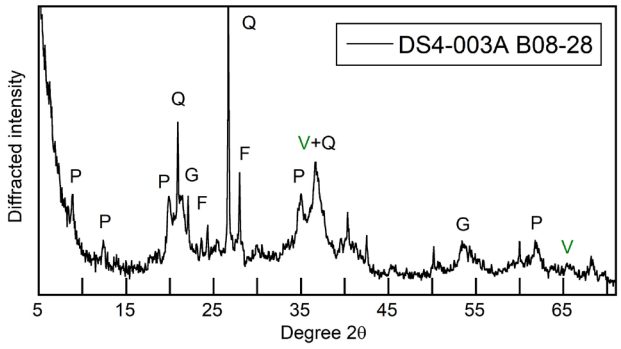
DS4-003A B08-28
Diffracted intensity
Degree 2θ
Q
P
G
F
V+Q
V

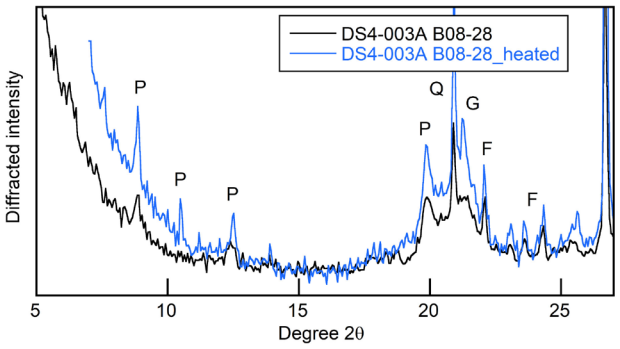
DS4-003A B08-28
DS4-003A B08-28_heated
Diffracted intensity
Degree 2θ
P
Q
G
F

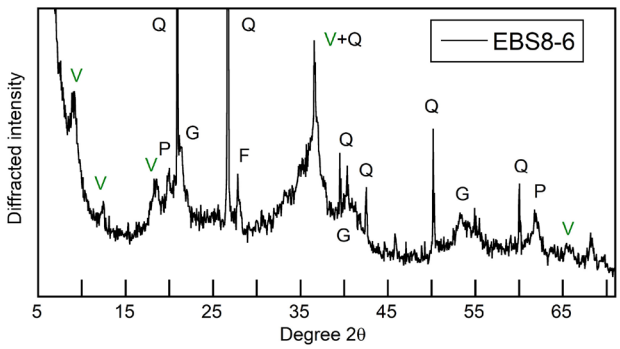
EBS8-6
Diffracted intensity
Degree 2θ
V
Q
P
G
F
V+Q

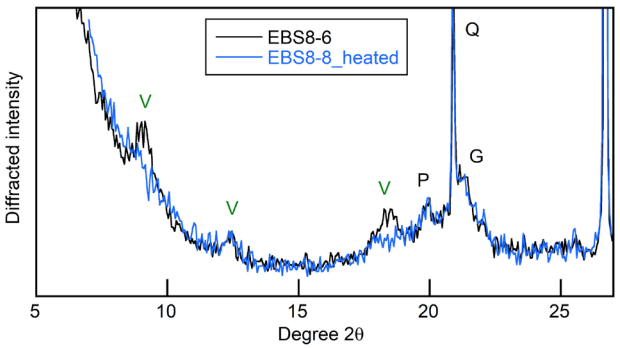
EBS8-6
EBS8-8_heated
Diffracted intensity
Degree 2θ
V
Q
G
P

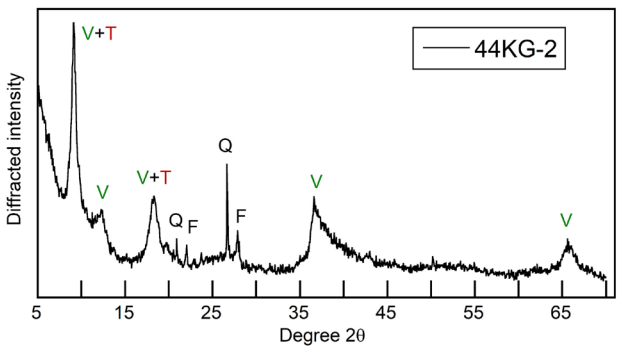
44KG-2
Diffracted intensity
Degree 2θ
V+T
V
Q
F

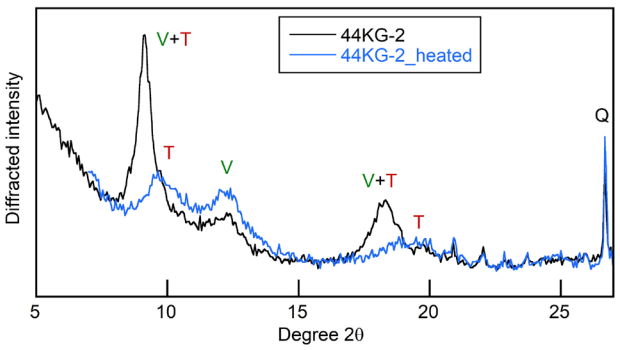
44KG-2
44KG-2_heated
Diffracted intensity
Degree 2θ
V+T
T
V
Q

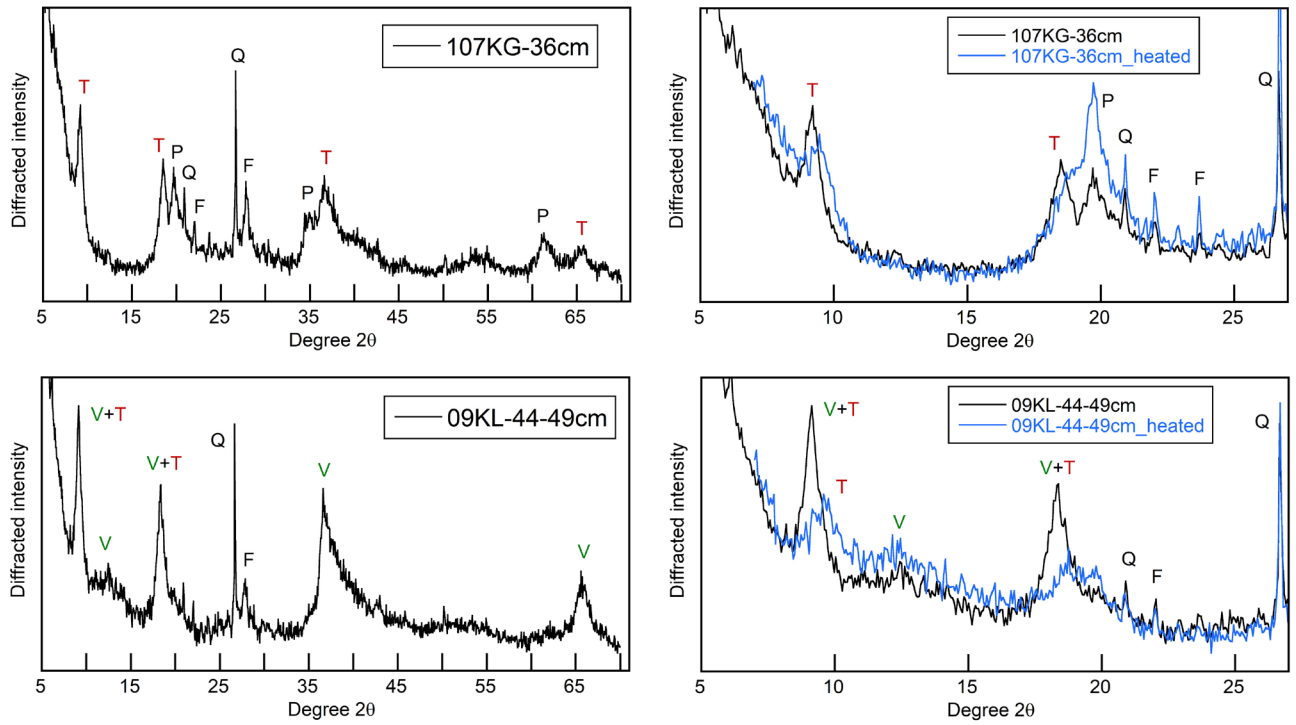

Figure S5. X-ray diffraction patterns of the FeMn crusts and nodules, with the exception of those measured previously by Wegorzewski et al.[13] 10 Å vernadite and todorokite were distinguished by dehydration at 110 °C in vacuum during 12 hours.

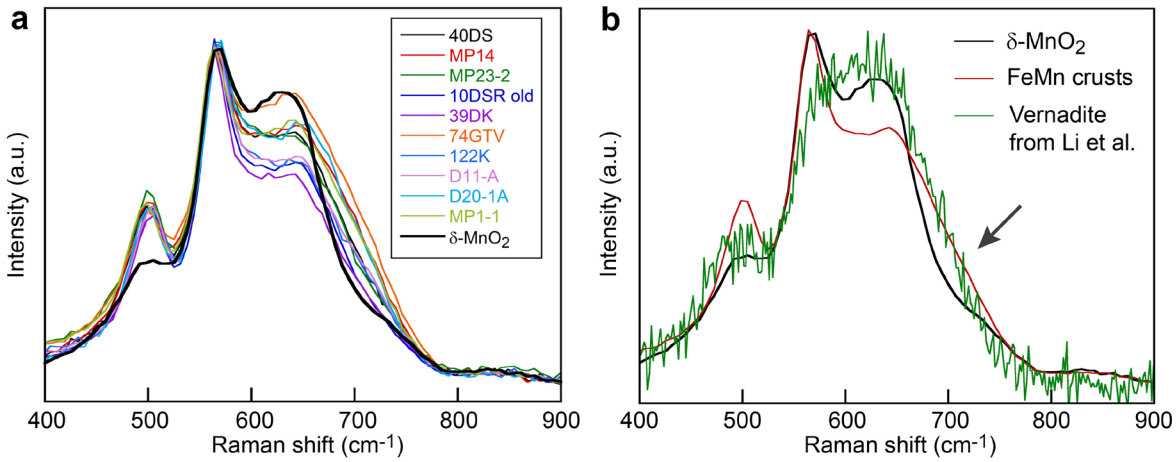

Figure S6. (a) Raman spectra of the FeMn crusts and δ-MnO_2. (b) Raman spectrum for Fe-rich vernadite layers of FeMn nodules from the Mariaa Trench measured by Li et al.[14]

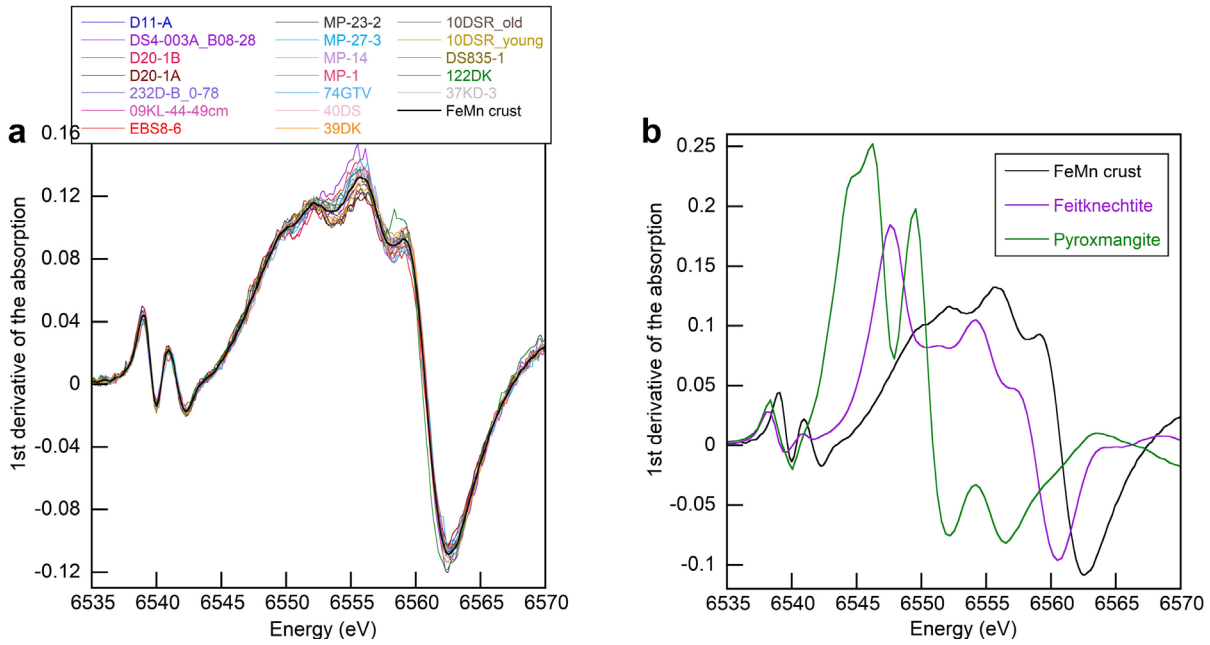

Figure S7. (a) First derivative of the 19 Mn-XANES spectra which were averaged to get a spectrum representative of the FeMn crusts. (b) XANES derivative of the FeMn crust spectrum with the spectra of a Mn(III) reference (feitknechtite, β-MnOOH) and a Mn(II) reference (pyroxmangite) showing the sensitivity of XANES spectroscopy to the oxidation state of Mn. The two reduced forms of Mn produce a shift to lower energy of the derivative. Their proportions were obtained by linear combination fitting (LCF) to an extended database of reference spectra under the constraint of non-negativity in the loadings (Combo fit).[15]

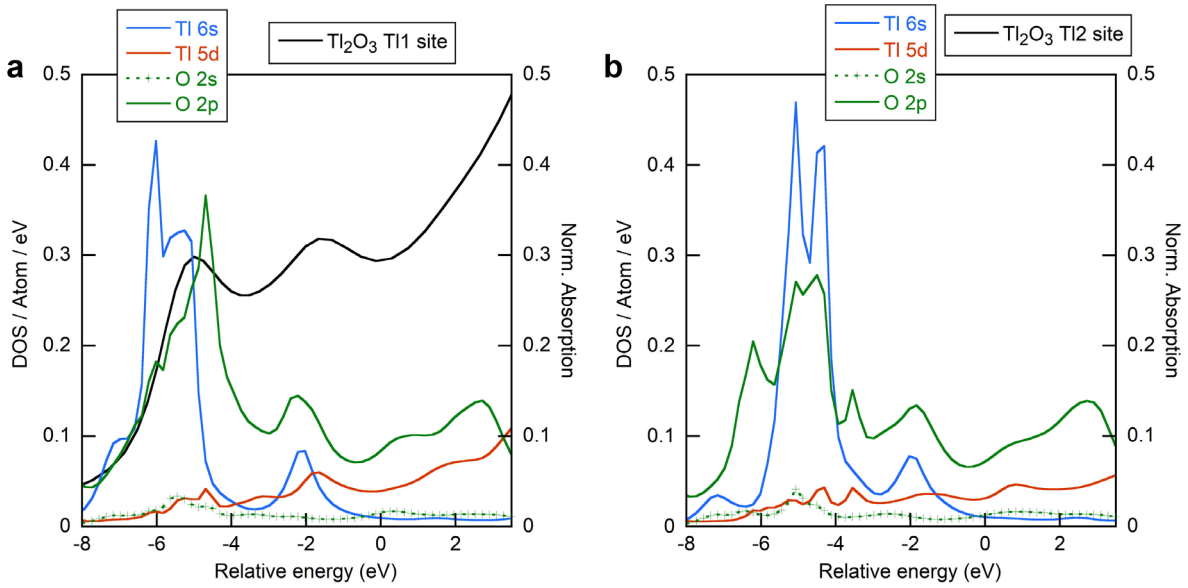

Figure S8. Thallium 5d and 6s and oxygen 2s and 2p empty density of states (DOS) of the Tl(1) (a) and Tl(2) (b) sites for Tl_2O_3. The Tl-O σ-bond is between a hybrid 6s5d state of the Tl atom and a hybrid 2sp state of the O atom. Tl 6s - O 2p mixing is the most pronounced, in agreement with valence-band photoemission and band-structure calculations.[16] The density of empty 6s states is higher at the Tl(2) site, which means that the probability of $2p_{3/2} \rightarrow 6s$ transitions is higher, and therefore the low-edge-peak more intense. In addition, the 6s states of Tl(2) are shifted to higher energy and as a result the 6s-5d hybridization is stronger, which also contributes to enhance the low-edge peak.

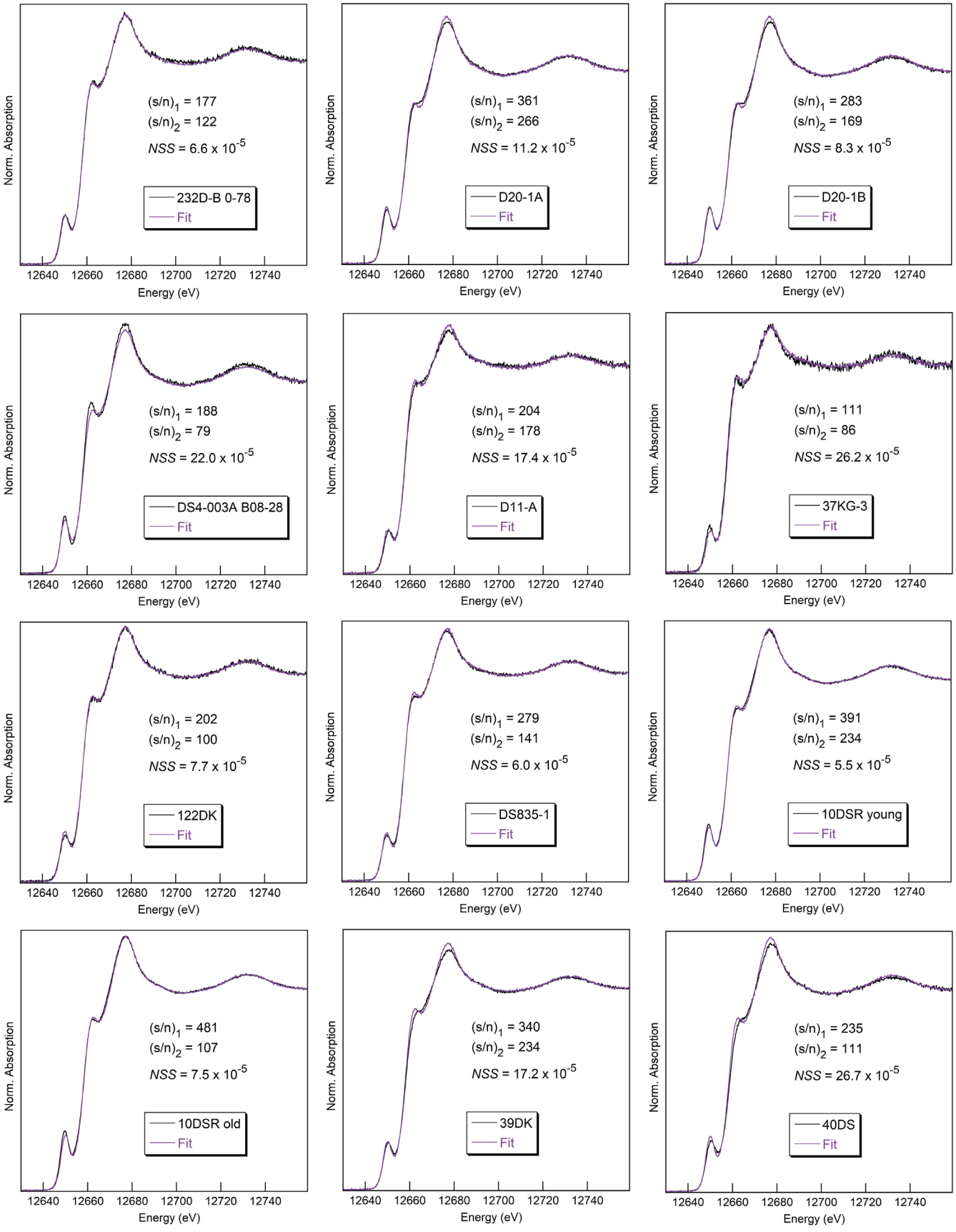
Norm. Absorption
Energy (eV)
12640 12660 12680 12700 12720 12740
(s/n)1 = 177
(s/n)2 = 122
NSS = 6.6 x 10-5
232D-B 0-78
Fit
(s/n)1 = 361
(s/n)2 = 266
NSS = 11.2 x 10-5
D20-1A
Fit
(s/n)1 = 283
(s/n)2 = 169
NSS = 8.3 x 10-5
D20-1B
Fit
(s/n)1 = 188
(s/n)2 = 79
NSS = 22.0 x 10-5
DS4-003A B08-28
Fit
(s/n)1 = 204
(s/n)2 = 178
NSS = 17.4 x 10-5
D11-A
Fit
(s/n)1 = 111
(s/n)2 = 86
NSS = 26.2 x 10-5
37KG-3
Fit
(s/n)1 = 202
(s/n)2 = 100
NSS = 7.7 x 10-5
122DK
Fit
(s/n)1 = 279
(s/n)2 = 141
NSS = 6.0 x 10-5
DS835-1
Fit
(s/n)1 = 391
(s/n)2 = 234
NSS = 5.5 x 10-5
10DSR young
Fit
(s/n)1 = 481
(s/n)2 = 107
NSS = 7.5 x 10-5
10DSR old
Fit
(s/n)1 = 340
(s/n)2 = 234
NSS = 17.2 x 10-5
39DK
Fit
(s/n)1 = 235
(s/n)2 = 111
NSS = 26.7 x 10-5
40DS
Fit

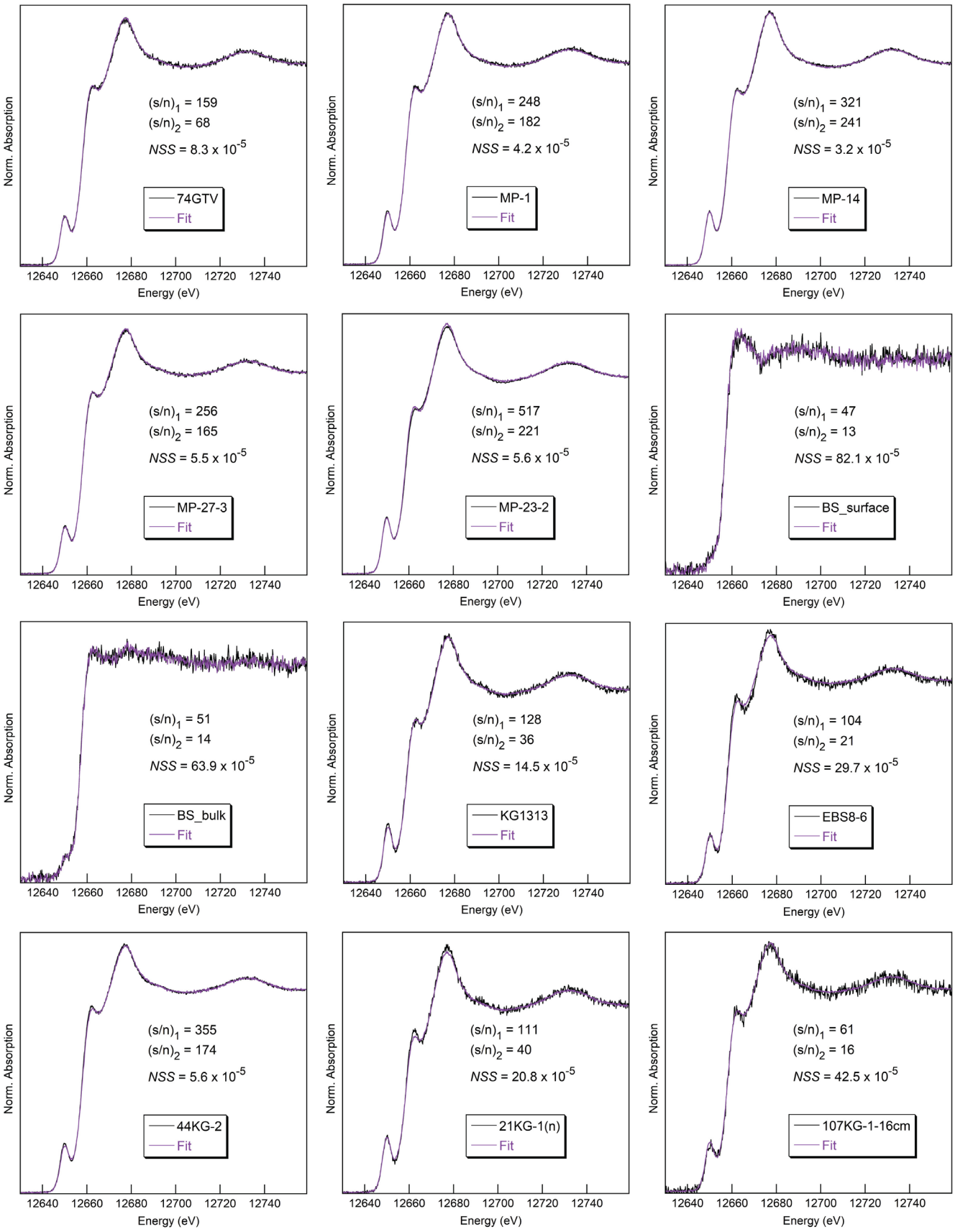
Norm. Absorption
Energy (eV)
12640 12660 12680 12700 12720 12740
(s/n)1 = 159
(s/n)2 = 68
NSS = 8.3 x 10-5
74GTV
Fit
(s/n)1 = 248
(s/n)2 = 182
NSS = 4.2 x 10-5
MP-1
Fit
(s/n)1 = 321
(s/n)2 = 241
NSS = 3.2 x 10-5
MP-14
Fit
(s/n)1 = 256
(s/n)2 = 165
NSS = 5.5 x 10-5
MP-27-3
Fit
(s/n)1 = 517
(s/n)2 = 221
NSS = 5.6 x 10-5
MP-23-2
Fit
(s/n)1 = 47
(s/n)2 = 13
NSS = 82.1 x 10-5
BS_surface
Fit
(s/n)1 = 51
(s/n)2 = 14
NSS = 63.9 x 10-5
BS_bulk
Fit
(s/n)1 = 128
(s/n)2 = 36
NSS = 14.5 x 10-5
KG1313
Fit
(s/n)1 = 104
(s/n)2 = 21
NSS = 29.7 x 10-5
EBS8-6
Fit
(s/n)1 = 355
(s/n)2 = 174
NSS = 5.6 x 10-5
44KG-2
Fit
(s/n)1 = 111
(s/n)2 = 40
NSS = 20.8 x 10-5
21KG-1(n)
Fit
(s/n)1 = 61
(s/n)2 = 16
NSS = 42.5 x 10-5
107KG-1-16cm
Fit

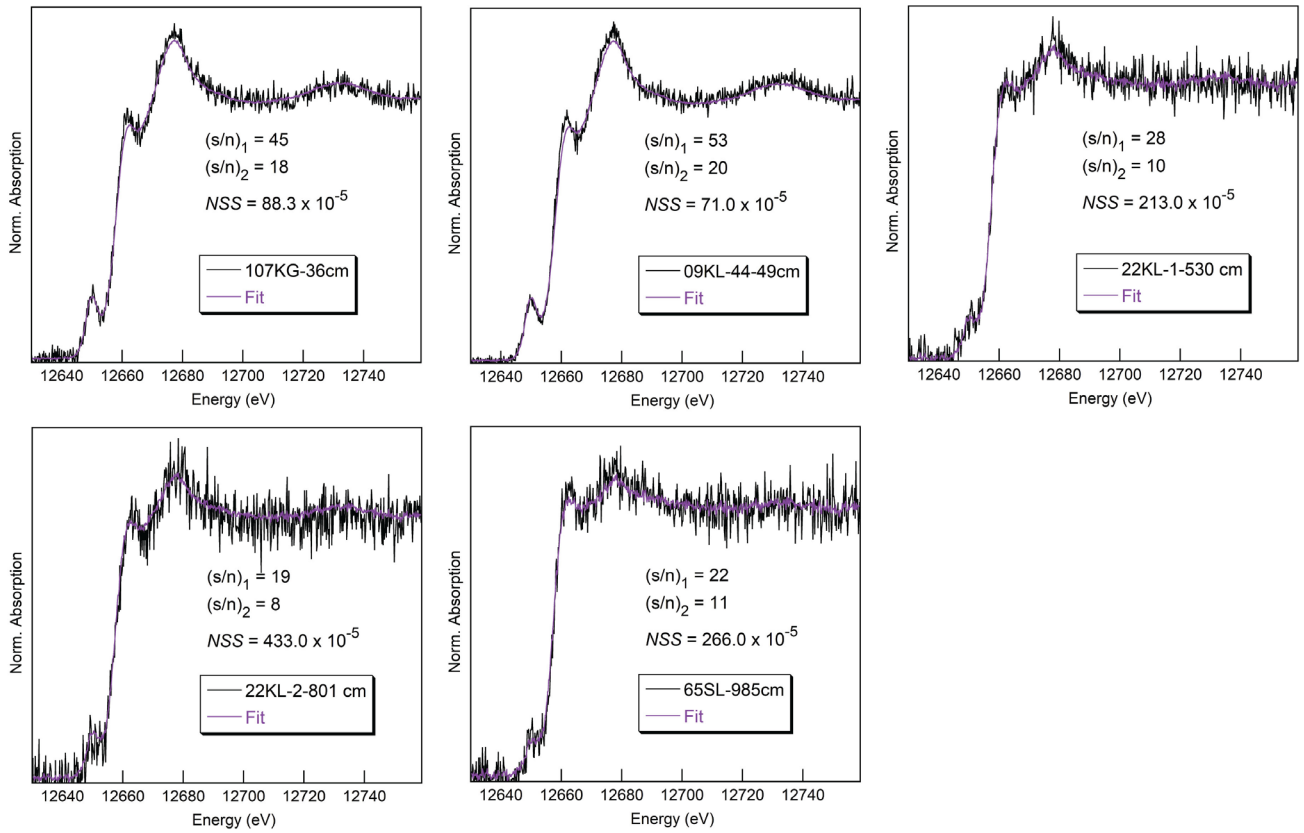

Figure S9. Plot of the 29 Tl L_3-edge HR-XANES spectra measured for this study with the best-fit spectra calculated with linear-combinations of the Tl(I) and Tl(III) endmembers, and with the signal-to-noise ratios.

Table S1. Location of the 29 FeMn samples

Cruise ID	Sample name	Latitude	Longitude	Water depth (m)
DODO	232D-B 0-78	05˚23.0'S	97˚29.0'E	4119-3558
RRKNOX06	D20-1A	13° 5' 60" S	87° 50' 60" E	3283
RRKNOX06	D20-1B	13° 5' 60" S	87° 50' 60" E	3283
HLY0905	DS4-003A B08-28	78° 39.6' N	158° 15.0' W	2200
AVON02	D11-A	0° 11.28' S	173° 39.6' E	1399
SO205	37KD-3	11°40.6`N	116°38.3`W	4006
SO83	122DK	24°53'N	21°42'W	1700-1800
POS235	DS835-1	30°09'N	14°444'W	1111-1230
SO66	10DSR young	4°10.10'S	174°51.20'W	1600
SO66	10DSR old	4°10.10'S	174°51.20'W	1600
SO33	39DK	09º11'N	164º50'W	1217
SO37	40DS	15º38'N	169º05'W	3049
SO92	74GTV	25°23.73'S	069°45.61'E	2808
SO193	MP-1	10º48.52'S	168º44.75'W	3672 - 4063
SO193	MP-14	13º41.76'S	161º27.28'W	3979 - 4237

SO193	MP-27-3	8º56.97'S	162º20.62'W	1982 - 2455
SO193	MP-23-2	9º30.02S	162º4.42'W	1222 - 1222
-	BS-surface	ca. 54°10'N	ca. 11°10'E	20
-	BS-bulk	ca. 54°10'N	ca. 11°10'E	20
SO79	KG1313	7°00'S	88°35'W	4150
SO237	EBS8-6	11°40.73`N -11°40.45`N	47°58.03`W - 47°59.00`W	4986
SO205	44KG-2	11°57.4`N	116°57.2`W	4188
SO240	21KG-1(n)	13°10.5´N	118°08.2`W	4288
SO240	107KG-1-16cm	11°50.1`N	116°32.9`W	4351
SO240	107KG-36cm	11°50.1`N	116°32.9`W	4351
SO240	09KL-44-49cm	13°10.5`N	118°10.1`W	4335
SO240	22KL-1-530 cm	13°10.5`N	118°08.2`W	4302
SO240	22KL-2-801 cm	13°10.5`N	118°08.2`W	4303
SO240	65SL-985cm	12°56.1`N	119°08.9`W	4293

Table S3. List of pure-valence references used in Combo fits

Standard	**Formula**	**Mn valence**
Pyrolusite	β-MnO_2	4.0
Ramsdellite	MnO_2	4.0
$Ca_2Mn_3O_8$	2/3 $Ca_2Mn_3O_8$ + 1/3 CaMnO3	4.0
KBi[a]	$K_{0.296}(Mn^{4+}_{0.926}\square_{0.074})O_2 \cdot 0.4H_2O$	4.0
Feitknechtite	β-MnOOH	3.0
Groutite/manganite	1/3 α-MnOOH + 2/3 γ-MnOOH	3.0
Manganite	γ-MnOOH	3.0
Mn_2O_3	Mn_2O_3	3.0
$MnPO_4$	$MnPO_4$	3.0
Hureaulite	$Mn_5(PO_4)_2(PO_3OH)_2 \cdot 4H_2O$	2.0
Rhodochrosite	$MnCO_3$	2.0
Manganosite	MnO	2.0
Pyroxmangite	$(Mn,Fe)SiO_3$	2.0
Tephroite	Mn_2SiO_4	2.0
$MnSO_{4(s)}$	$MnSO_4 \cdot xH_2O$	2.0

[a]The TEY spectrum was used in the Combo fits, because this reference was unavailable.

Table S5. Tl concentration, percentage of Tl(III) and Tl(I) and precision, fit residual, and signal to noise ratio of the HR-XANES spectra

ID	[Tl] ppm	%Tl(III)	%Tl(I)	Precision	NSS x10^5	$(s/n)_1$[a]	$(s/n)_2$[a]
232D-B 0-78	1.5	79	21	3	6.6	177	122
D20-1A	190	100	0	3	11.2	361	266
D20-1B	151	100	0	3	8.3	283	169
DS4-003A B08-28	47	94	6	5	22.0	188	79
D11-A	157	66	34	5	17.4	204	178
37KD-3	103	62	38	6	26.2	111	86
122DK	46	79	21	3	7.7	202	100
DS835-1	127	74	26	3	6.0	279	141
10DSR young	252	88	12	3	5.5	391	234
10DSR old	319	91	9	3	7.5	481	107
39DK	278	77	23	4	17.2	340	234
40DS	135	91	9	6	26.7	235	111
74GTV	39	79	21	3	8.3	159	68
MP-1	97	85	15	3	4.2	248	182
MP-14	157	88	12	2	3.2	321	241
MP-27-3	97	75	25	3	5.5	256	165
MP-23-2	283	95	5	3	5.6	517	221
BS-surface	2	0	100	9	82.1	47	13
BS-bulk	4	19	82	9	63.9	51	14
KG1313	22	96	4	4	14.5	128	36
EBS8-6	10	77	23	6	29.7	104	21
44KG-2		74	26	3	5.6	355	174
21KG-1(n)	44	100	0	5	20.8	111	40
107KG-1-16cm	11	79	21	6	42.5	61	16
107KG-36cm	5	77	23	11	88.3	45	18
09KL-44-49cm	15	78	22	9	71.0	53	20
22KL-1-530 cm	2	39	61	15	213.0	28	10
22KL-2-801 cm	2	49	50	21	433.0	19	8
65SL-985cm	2	31	69	18	266.0	22	11

[a]The formulae used to calculate the signal-to-noise ratios are given in the caption of Figure S4

Table S6. Structural parameters of the Tl(III)-TCS and Tl(III)-DES complexes on the MP23-2 crust derived from the Tl L_3-edge EXAFS analysis

Tl-O			Tl-Mn				
R (Å)	*CN*	σ^2 (Å)	*R* (Å)	*CN*	σ^2 (Å)	ΔE_0 (eV)	*Res*
2.18	3.6[a]	0.007[b]	3.22	0.9	0.011[b]	-6.1[b]	6.3[c]
2.33	2.4[a]	0.007[b]	3.66	3.1	0.011[b]	-6.1[b]	-

[a]Coordination number fixed to 6. [b]Parameters constrained to suppress correlations between σ and *CN*.
[c]*Res* = $[\Sigma(|\chi_{exp} - \chi_{fit}|)/\Sigma(|\chi_{exp}|)]$ x 100. Accuracy: *R* = 0.02 Å, *CN* = 20%.